POLITECNICO DI TORINO
Repository ISTITUZIONALE

A Volume-of-Fluid method for multicomponent droplet evaporation with Robin boundary conditions

Original
A Volume-of-Fluid method for multicomponent droplet evaporation with Robin boundary conditions / Zamani Salimi, Salar; Scapin, Nicolò; Popescu, Elena-Roxana; Costa, Pedro; Brandt, Luca. - In: JOURNAL OF COMPUTATIONAL PHYSICS. - ISSN 0021-9991. - 514:(2024). [10.1016/j.jcp.2024.113211]

Availability:
This version is available at: 11583/2990400 since: 2024-07-05T12:42:38Z

Publisher:
Elsevier

Published
DOI:10.1016/j.jcp.2024.113211

Terms of use:

This article is made available under terms and conditions as specified in the corresponding bibliographic description in the repository

Publisher copyright
Elsevier postprint/Author's Accepted Manuscript

© 2024. This manuscript version is made available under the CC-BY-NC-ND 4.0 license
http://creativecommons.org/licenses/by-nc-nd/4.0/.The final authenticated version is available online at:
http://dx.doi.org/10.1016/j.jcp.2024.113211

(Article begins on next page)

06 October 2024

Journal of Computational Physics 514 (2024) 113211

Contents lists available at ScienceDirect

Journal of Computational Physics

journal homepage: www.elsevier.com/locate/jcp

A Volume-of-Fluid method for multicomponent droplet evaporation with Robin boundary conditions

Salar Zamani Salimi [a,*], Nicolò Scapin [b,c], Elena-Roxana Popescu [d], Pedro Costa [e], Luca Brandt [a,c]

[a] Department of Energy and Process Engineering, Norwegian University of Science and Technology (NTNU), Trondheim, Norway
[b] Department of Mechanical and Aerospace Engineering, Princeton University, NJ, USA
[c] FLOW, Department of Engineering Mechanics, KTH, SE-10044 Stockholm, Sweden
[d] Flow Technology Group, SINTEF Industry, Trondheim, Norway
[e] Process & Energy Department, TU Delft, Leeghwaterstraat 39, 2628CB, Delft, the Netherlands

ARTICLE INFO

Keywords:
Volume-of-Fluid method
Robin boundary condition
Phase change
Multicomponent liquid droplet

ABSTRACT

We propose a numerical method tailored to perform interface-resolved simulations of evaporating multicomponent two-phase flows. The novelty of the method lies in the use of Robin boundary conditions to couple the transport equations for the vaporized species in the gas phase and the transport equations of the same species in the liquid phase. The Robin boundary condition is implemented with the cost-effective procedure proposed by Chai et al. [1] and consists of two steps: (1) calculating the normal derivative of the mass fraction fields in cells adjacent to the interface through the reconstruction of a linear polynomial system, and (2) extrapolating the normal derivative and the ghost value in the normal direction using a linear partial differential equation. This methodology yields a second-order accurate solution for the Poisson equation with a Robin boundary condition and a first-order accurate solution for the Stefan problem. The overall methodology is implemented in an efficient two-fluid solver, which includes a Volume-of-Fluid (VoF) approach for the interface representation, a divergence-free extension of the liquid velocity field onto the entire domain to transport the VoF, and the temperature equation to include thermal effects. We demonstrate the convergence of the numerical method to the analytical solution for multicomponent isothermal evaporation and observe good overall computational performance for simulating non-isothermal evaporating two-fluid flows in two and three dimensions.

1. Introduction

Multiphase flows that encompass heat and mass transfer play a pivotal role in diverse industrial applications, such as power generation, combustion engines, and cooling and refrigeration systems. Employing predictive simulations to unravel the intricate effects of phase change on these engineering systems is crucial because experiments still have limited access to the flow details. However, the simultaneous exchange of mass, momentum, and energy introduces considerable numerical complexities, amplifying the challenges associated with modeling interfacial flows. Moreover, the presence of multiple species in liquid droplets is more of a norm than an exception, prompting extensive investigations across various engineering applications. Existing models often hinge

* Corresponding author.
E-mail address: salar.z.salimi@ntnu.no (S. Zamani Salimi).

https://doi.org/10.1016/j.jcp.2024.113211
Received 7 February 2024; Received in revised form 20 May 2024; Accepted 17 June 2024

Available online 20 June 2024
0021-9991/© 2024 The Author(s). Published by Elsevier Inc. This is an open access article under the CC BY license (http://creativecommons.org/licenses/by/4.0/).

on the assumption of spherical symmetry, typically overlooking the influence of surface tension and droplet deformation [2,3], and neglecting the mutual interactions of evaporating droplets in instances of larger initial volume fraction. While these simplifications prove suitable for scenarios involving droplets in microgravity and under dilute conditions, where buoyancy, deformation, and droplet-droplet interactions have negligible effects – such as in chemical reactions and combustion [4] – there persists a demand for multidimensional models. Such models are imperative to provide a more accurate depiction of phase transitions in turbulent flows, particularly in non-dilute conditions, where the inherent constraints of existing models become apparent.

Numerical methods for interfacial flow can be divided into two broad categories, *interface-tracking* and *interface-capturing* methods, and most of the approaches developed so far have been extended to account for phase change.

Interface-tracking (or front-tracking, FT) methods demonstrate the potential for achieving remarkable precision in computing the interface properties, i.e., normal vector and curvature, thanks to using Lagrangian markers to describe the interface motion. For this reason, the FT method has been adapted to study boiling films [5–8], evaporating droplets [9] even with chemical reactions [10]. However, the practical use of the FT methods in more complex configurations is currently limited by two drawbacks: (i) poor conservation properties for large mismatch in the thermophysical properties of the phases and for large topological changes of the interface [11,12] and (ii) difficulties in achieving parallel scalability in modern HPC architectures [13].

Interface-capturing methods, particularly those based on the Volume-of-Fluid (VoF) and the Level-Set (LS) method, have gained widespread application, owing to their implicit representation of interfaces and the ability to achieve improved conservation properties, especially in the presence of significant thermophysical properties mismatches between phases. Despite these advantages, challenges arise from the implicit interface representation and the lack of a precise interface position, necessitating specific treatments for accurately computing mass and energy exchanges at the interface. One of the earliest applications of interface-capturing methods in phase-changing flows is based on a level-set method, notably in the context of film boiling [14]. The Level-Set method has become increasingly popular in this domain due to its coupling with the ghost fluid method, which facilitates the imposition of interfacial jump conditions [15–17]. This coupling is particularly advantageous in enhancing phase change predictions, especially when the interface is well-resolved. The application of the method has been extended to evaporating flows [18] and combined boiling and evaporation scenarios [19–21]. Despite its potential for high accuracy, the Level-Set function is not a conserved quantity, and issues related to poor conservation behavior have been reported [20], especially when the computational mesh lacks sufficient refinement to resolve liquid structures. Recent studies have addressed this issue with Level-Set methods (in the absence of phase change) by incorporating mass-correction steps. These consist of redistributing the lost mass in the vicinity of the interface, accounting for factors such as local interface curvature [22,23].

Another commonly employed technique for simulating multiphase flows is the VoF method, which is particularly advantageous because it potentially allows to achieve exact mass conservation properties irrespective of the employed grid resolution. Despite this advantage, the use of the VoF method for phase-changing flows has been limited by the intrinsic challenge in defining a suitable velocity to advect the VoF color function. Indeed, the presence of phase change introduces a discontinuity in the velocity field, which makes it unsuitable as interface velocity. Therefore, practically all the VoF-based methods developed so far had to devise a strategy to transport the interface stably and accurately. In the earliest attempts [24,25], the interface velocity has been obtained by combining the solution of the momentum equation with different compression schemes to avoid excessive interface smearing and distortion induced by the velocity discontinuity. A geometric-based VoF method was first employed to investigate evaporating droplets [26], where an iterative approach was developed to handle the calculation of a volume source due to mass transfer, applied locally in interface cells and without regularization. However, the velocity disparity between the interface and the liquid phase was overlooked. Later, the same group developed a consistent method to simulate evaporation processes for a large range of ambient conditions, from supercooled droplets to extreme environments with high evaporation rates [27]. For low gas diffusivities, a fixed-point expression is introduced to establish consistency between the interface temperature, saturation pressure, the rate of phase change, and the rate of interfacial mass diffusion [28]. This is done by assuming an error function profile for the sub-grid scale temperature. The concept of consistency is also leveraged to apply the fixed-point iteration directly to a first-order discretization of the interfacial fluxes defined on the geometrically reconstructed interface, thereby achieving a discretely consistent prediction of phase change. In more recent studies, the problem of the velocity discontinuity and the suitable definition of the interface velocity has been circumvented using different strategies, either with the solution of an additional Poisson/Helmholtz equation to define an extended liquid velocity [29–33] or by shifting the Stefan flow away from the interfacial cell while keeping it within the first two-three layers of pure gas/liquid cells [34–36]. All these works have been primarily targeting thermally-induced or mass-transfer-induced phase change of single-component droplets, which simplifies the calculation of the vaporization rate. At the same time, less effort has been devoted to considering the case of liquid droplets comprising multiple species.

Extending phase-change models to systems involving multiple components presents two main challenges: *(a)* the interfacial mass flux rate calculation is not trivial since the species mass fractions at the interface are not known a prior, even in an isothermal condition as in pure droplets; *(b)* the species mass fraction fields must be transported in both liquid and gas phases, considering boundary conditions for both vapor and liquid fields at the interface.

Here, we introduce a numerical model designed for conducting interface-resolved simulations of multicomponent phase-changing flows using the volume-of-fluid method. The novelty of the method lies in the strategy employed to couple the transport equations governing the vaporized species in the gas phase with the transport equations describing the species in the liquid phase. The first set of equations, i.e. vaporized species in the gas phase, are solved with a Dirichlet boundary condition at the interface. This condition is derived under thermodynamic equilibrium and computed from an appropriate equation of state, e.g. the Clausius-Clapeyron relation or Span-Wagner equation of state. The second set of equations, i.e. species in the liquid phase, is solved with a Robin boundary condition, which is constructed to ensure that each contribution to the total mass-flux from the individual vaporized species is

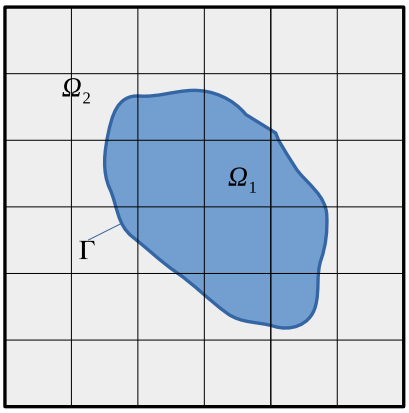

Fig. 1. 2D sketch of the physical domain. The two phases, evolving in the two disjoint subdomains Ω_1 and Ω_2, are separated by an infinitesimally thin interface Γ.

accounted for. Note that Cipriano et al. [33] recently proposed a second-order accurate alternative procedure to couple the jump conditions for the vaporized species in the gas domain and the same species in the liquid domain with the corresponding transport equations. The method employs the information, i.e. the vaporized mass fraction and its interfacial gradients, at the previous timestep to compute each partial mass-flux and the total exchange mass-flux. In our work, this "explicit" coupling is made implicit by the use of the Robin boundary condition. The proposed methodology of this work is then coupled with the efficient two-fluid solver for single-component evaporating flows described in our previous work [29]. The solver consists of two parts. First, it includes an algebraic VoF function to capture the interface motion. The VoF function is advected with a smooth interface velocity that consists of two terms: a divergence-free extended liquid velocity field and an irrotational term attributed to phase change, following the approach in [29]. Next, it incorporates an efficient, FFT-based finite-difference Navier-Stokes solver [37]. The overall methodology is validated against benchmarks of increasing complexities. First, we verify the proposed algorithm for the Robin boundary condition against a Poisson and a Stefan problem. Next, we validate the overall numerical algorithm against an analytical solution for the isothermal evaporation of a static bi-component droplet. Finally, we demonstrate the ability of the method to simulate evaporating flows in two complex configurations: (a) a settling droplet under gravity, which undergoes evaporation and deformation near a solid boundary, (b) a three-dimensional evaporating droplet in homogeneous isotropic turbulence. This last configuration shows the potentialities of the method to tackle multiphase and multicomponent turbulent flows.

This paper is organized as follows. The mathematical model is described in section 2, while section 3 describes the numerical discretization of the different transport equations. The resulting model is validated against several benchmarks in section 4. Finally, conclusions are drawn in section 5.

2. Mathematical formulation

We consider a system comprising two immiscible Newtonian phases: a liquid phase, denoted by 1, and a gas phase, denoted by 2. The liquid phase is composed of N_v liquid species, while the gas phase is an ideal mixture composed of N_v vaporized species and an inert gas. These two phases are separated by an infinitesimally thin interface Γ, through which the transfer of energy, momentum, and mass occurs. The process of evaporation is driven by the partial pressure of each vaporized species in phase 2. As shown in Fig. 1, the two phases occupy two disjoint subdomains Ω_1 and Ω_2, separated by a lower dimensional interface Γ.

A phase indicator function H is utilized to implicitly represent each phase at location $\mathbf{x}$ and time t:

$$H(\mathbf{x},t) = \begin{cases} 1 & \text{if } \mathbf{x} \in \Omega_1, \\ 0 & \text{if } \mathbf{x} \in \Omega_2. \end{cases} \tag{1}$$

The function H is governed by the following transport equation [38,8]:

$$\frac{\partial H}{\partial t} + \mathbf{u}_\Gamma \cdot \nabla H = 0, \tag{2}$$

where $\mathbf{u}_\Gamma = (u_\Gamma, v_\Gamma, w_\Gamma)$ is the interface velocity, which in the presence of phase change can be computed from the Rankine-Hugoniot relations:

$$\dot{m} = \rho_1(\mathbf{u}_1 - \mathbf{u}_\Gamma)\cdot\mathbf{n} = \rho_2(\mathbf{u}_2 - \mathbf{u}_\Gamma)\cdot\mathbf{n}. \tag{3}$$

In expression (3), $\mathbf{u}_{i=1,2}$ are the velocities on the two sides of the interface, $\rho_{i=1,2}$ are the mass densities and $\mathbf{n}$ is the normal vector defined as $\mathbf{n} = \nabla H/|\nabla H|$. As commonly done in the one-fluid formulation for multiphase flow [38], the phase indicator H is employed to define also the one-fluid velocity, i.e. $\mathbf{u} = H\mathbf{u}_1 + (1-H)\mathbf{u}_2$, and the generic volumetric thermophysical property η (the mass density ρ, the dynamic viscosity μ, the thermal conductivity λ and the specific heat capacity at constant pressure c_p), which is evaluated using an arithmetic mean, i.e. $\eta = \eta_1 H + \eta_2(1-H)$. In the present work, the bulk values of each η, i.e. $\eta_{i=1,2}$,

are assumed constant and uniform. This assumption can be relaxed as shown in [39,40] for single-component evaporation without major modifications of the algorithm described in the next sections.

2.1. Navier-Stokes equations

The interfacial mass flux, $\dot{m}$, arising from phase change leads to a jump in the velocity field $\mathbf{u}$, formally expressed in equation (3). This affects the velocity divergence (or divergence constrain), derived by taking the divergence operator of $\mathbf{u}$, assuming uniform and constant bulk densities, and using equation (3). This constrain finally reads [38]:

$$\nabla \cdot \mathbf{u} = \dot{m} \left(\frac{1}{\rho_2} - \frac{1}{\rho_1} \right) \delta_\Gamma, \tag{4}$$

where $\delta_\Gamma \equiv \delta(\mathbf{x} - \mathbf{x}_\Gamma)$ is a three-dimensional Dirac delta function, non-zero at the interface location $\mathbf{x}_\Gamma$. The flow is assumed to be incompressible and, therefore, the Navier-Stokes equation, representing the conservation of momentum in the system, can be written as follows:

$$\rho \left(\frac{\partial \mathbf{u}}{\partial t} + \mathbf{u} \cdot \nabla \mathbf{u} \right) = -\nabla p + \nabla \cdot \left(\mu \left(\nabla \mathbf{u} + \nabla \mathbf{u}^T \right) \right) + \rho \mathbf{g} + \sigma \kappa \delta_\Gamma \mathbf{n}, \tag{5}$$

where p is the hydrodynamic pressure field and $\mathbf{g}$ is the gravitational acceleration; the right-most term accommodates the discontinuity in stress due to surface tension, which is computed via the standard continuum surface force (CSF) method with σ being the surface tension coefficient. The curvature surface field κ is defined using the normal vector, $\kappa = \nabla \cdot \mathbf{n}$ (pointing from the liquid toward the gas). It should be noted that, for the model proposed here, the momentum equation (5) is coupled only with the divergence constraint (4), i.e. the density is only a function of the phase, and not directly of temperature. Accordingly, the velocity field must respect the constraint (4), which directly depends on the total interfacial mass flux.

2.2. Species transport equations

The liquid phase is composed of N_v species, which can be both in liquid state, confined in the domain Ω_1, and in a vapor state, confined in Ω_2 together with the inert component. Therefore, for each species, we need two variables, Y_k^l and Y_k^g, which represent the mass of the species k in the vapor and liquid state over the total mass contained in Ω_1 and Ω_2. Clearly, $\sum_{k=1}^{N_v} Y_k^l = 1$ and $\sum_{k=1}^{N_v} Y_k^g + Y_0 = 1$ with Y_0 the mass fraction of the inert component, denoted with the index 0. It is also useful to define the corresponding molar mass fraction, which can be conveniently computed from $Y_k^{l,g}$ as

$$X_k^{l,g} = Y_k^{l,g} \frac{M_m^{l,g}}{M_k}, \tag{6}$$

where M_k is the molar mass of the species k (in vapor or liquid phase) and $M_m^{l,g}$ is the molar mass of the mixture in the liquid (l) or in the gas (g). The mixture molar mass $M_m^{l,g}$ can be computed using a simple mixture rule (valid for ideal mixtures composed of ideal gases [41]). In particular, for M_m^l we have

$$M_m^l = \left(\sum_{k=1}^{N_v} \frac{Y_k^l}{M_k} \right)^{-1}, \tag{7}$$

whereas for M_m^g

$$M_m^g = \left(\sum_{k=1}^{N_v} \frac{Y_k^g}{M_k} + \frac{Y_0}{M_0} \right)^{-1}. \tag{8}$$

Note that equations (7), (8) simply differ for the inclusion of the inert species in the gas mixture. Each $Y_k^{g,l}$ is governed by the same standard convection-diffusion equation:

$$\frac{\partial Y_k^{l,g}}{\partial t} + \mathbf{u} \cdot \nabla Y_k^{l,g} = D_k^{l,g} \nabla^2 Y_k^{l,g}, \tag{9}$$

where $D_k^{l,g}$ is the diffusion coefficient in the liquid or gas phase, which we assume constant, as the other thermophysical properties. Clearly, the equations for Y_k^l is valid in Ω_1, while Y_k^g is defined in Ω_2. At the interface Γ, they are naturally coupled by the jump condition for the interfacial gradients, which reads [18,42,33]:

$$\dot{m}_k = \dot{m} Y_{k,\Gamma}^l + \rho_l D_k^l \nabla Y_k^l \cdot \mathbf{n} = \dot{m} Y_{k,\Gamma}^g + \rho_g D_k^g \nabla Y_k^g \cdot \mathbf{n}, \tag{10}$$

where $\dot{m}_k$ is the partial mass-flux, $\dot{m}$ is the total mass-flux and $Y^{l,g}_{k,\Gamma}$ are the values of the mass fraction on the liquid and the gas side of the interface. Note that $Y^{l}_{k,\Gamma}$ and $Y^{g}_{k,\Gamma}$ are not necessarily equal. The total mass-flux $\dot{m}$ in equation (10) can be computed by applying the summation operator $\sum_{k=1}^{N_v}$ to equation (10). Since $\sum_{k=1}^{N_v} Y^{l,g}_{k,\Gamma} = 1$ and $\sum_{k=1}^{N_v} \rho_g D^l_k \nabla Y^l_{k,\Gamma} \cdot \mathbf{n} = 0$ by definition [42,33], after some manipulations $\dot{m}$ can be written as

$$\dot{m} = \frac{\sum_{k=1}^{N_v} \rho_g D^g_k \nabla Y^g_k \cdot \mathbf{n}}{1 - \sum_{k=1}^{N_v} Y^g_{k,\Gamma}}. \tag{11}$$

$Y^g_{k,\Gamma}$ in equations (10) and (11) is assumed fixed, through a Dirichlet boundary condition at the interface Γ, and evaluated under the assumption that the interface is at saturation. By introducing the saturation vapor pressure $p^{sat}_{k,\Gamma}$, the mass fraction at the interface $Y^g_{k,\Gamma}$ for multicomponent liquids can be expressed as (see Appendix A for a derivation):

$$Y^g_{k,\Gamma} = \frac{p^{sat}_{k,\Gamma} M_k X^l_{k,\Gamma}}{p_t M_g + \sum_{k=1}^{N_v} p^{sat}_{k,\Gamma}(M_k - M_0) X^l_{k,\Gamma}}, \tag{12}$$

where p_t is the total pressure of the mixture and is taken equal to the thermodynamic pressure. It is important to remark that, as shown in equation (12), $Y^g_{k,\Gamma}$, is not only a function of the partial pressure (as for single-component droplets), but also of the local concentration of the liquid species. Assuming thermodynamic equilibrium at the interface, it is possible to predict $p^{sat}_{k,\Gamma}$ via the local interface temperature, T_Γ, through an equation of state. In this work, we employ the Span-Wagner relation [43], which reads

$$p^{sat}_{k,\Gamma} = p_{c,k} \exp\left[(A_1 \tau_{sp} + A_2 \tau^{1.5}_{sp} + A_3 \tau^{2.5}_{sp} + A_4 \tau^{5}_{sp})(1 - \tau_{sp})\right], \tag{13}$$

where $p_{c,k}$ and $T_{c,k}$ refer to the critical pressure and temperature of each species. In Eq. (13), $\tau_{sp} = 1 - T_\Gamma / T_{c,k}$ is the Span-Wagner parameter and the coefficients $A_{i=1,4}$ depend on the substance under consideration. Once $\dot{m}$ and $Y^g_{k,\Gamma}$ are known, the partial mass-flux of each species $\dot{m}_k$ is immediately available using equation (10) on the gas side of the interface. Conversely, the relation (10) is valid on the liquid side of the interface and serves a Robin boundary condition for the transport equations (9) for Y^l_k. Thus, the system of equations (9), (10), (11) and (12) provides a new strategy to handle multicomponent evaporation, which can be summarized as follows

- Solve N_v equations of the form (7) for the mass fraction Y^g_k in the gas phase, Ω_2, with a Dirichlet boundary condition at the interface Γ. The Dirichlet condition is provided by equation (12) together with an equation of state for the saturation pressure (13);
- Solve N_v equations of the form (7) for the mass fraction Y^l_k in the liquid phase, with a Robin boundary condition at the interface Γ. The Robin condition is provided by the left-hand side of equation (10).

2.3. Heat transport equation

In the context of the one-fluid formulation, the principle of thermal energy conservation can be represented by the following equation:

$$\rho c_p \left(\frac{\partial T}{\partial t} + \mathbf{u} \cdot \nabla T \right) = \nabla \cdot (\lambda \nabla T) - \dot{m} h_{lv} \delta_\Gamma + \sum_{k=1}^{N_v} \rho D^g_k (c^{vap}_{p,k} - c_{p2}) \nabla T \cdot \nabla Y_k (1 - H), \tag{14}$$

where viscous dissipation has been disregarded. In Eq. (14), T represents the temperature field, $c^{vap}_{p,k}$ denotes the specific heat capacity of vaporized liquid species, and λ refers to the thermal conductivity. The last two terms on the right-hand-side of equation (14) quantify the discontinuity in enthalpy resulting from phase change, attributed primarily to latent heat h_{lv}, but also to the differences in specific heat between the inert gas and the vaporized liquid components. It is important to note that integrating Eq. (14) across Γ yields a straightforward derivation of the jump in heat flux across the interface.

2.4. Non-dimensional parameters

The governing equations (4), (5), (9), (11) and (14) can be recast into a dimensionless form by introducing a reference velocity u_{ref}, a reference length l_{ref}, and temperature T_{ref}. The resulting dimensionless governing parameters are

$$\mathrm{Re} = \frac{\rho_2 u_{ref} l_{ref}}{\mu_2}, \quad \mathrm{We} = \frac{\rho_2 u^2_{ref} l_{ref}}{\sigma}, \quad \mathrm{Fr} = \frac{u^2_{ref}}{l_{ref} |\mathbf{g}|}, \quad \mathrm{Pr} = \frac{\mu_2 c_{p2}}{\lambda_2}, \quad \mathrm{Sc}^g_k = \frac{\mu_2}{D^g_k \rho_2},$$

$$\mathrm{Sc}_k^l = \frac{\mu_1}{D_k^l \rho_1}, \quad \mathrm{Ste} = \frac{c_{p2} T_{ref}}{h_{lv}}, \quad r_{M,k} = \frac{M_k}{M_0}, \quad r_\eta \equiv \frac{\eta_1}{\eta_2},$$

where Re, We, Fr, Pr, Sc_k^g, Sc_k^l, Ste, $r_{M,k}$ and r_η are the Reynolds, Weber, Froude, Prandtl, gas phase Schmidt number (for each gas components), liquid phase Schmidt number (for each liquid components), Stefan number, Molar mass ratio (for individual liquid species) and the ratio of the different thermophysical properties, r_η, where the property η can be ρ, μ, c_p or λ. Note again, that, in this study, all the thermophysical properties are assumed to be uniform and constant.

3. Numerical method

The numerical methodology proposed for solving the governing equations, presented in section 2, follows six steps: *(1)* the interface reconstruction and advancement with the volume-of-fluid method and the reconstruction with the Level-set method; *(2)* the discretization of the vapor mass fraction equations and the calculation of the interfacial mass fluxes; *(3)* the solution of the liquid mass fraction transport equation using a Robin boundary condition; *(4)* the discretization of the energy equation; *(5)* the solution of the momentum equation with a pressure-correction method, *(6)* the reconstruction of the interface velocity. The governing equations are solved on a Cartesian regular grid with uniform grid spacing in the three directions x, y and z. Note that the spacing along x is computed as $\Delta x = l_x / N_x$ with l_x and N_x the domain dimension and the number of grid cells in the x direction, respectively. A similar definition applies to y and z directions. The flow variables are stored in the computational grid using a staggered arrangement, i.e. all scalar fields are stored at the cell centers, whereas the components of the velocity field are stored at the corresponding cell faces.

3.1. Interface representation

The first step of the time-marching algorithm consists of the interface transport. The volume fraction ϕ for each cell within the computational domain is defined using the indicator function H as follows:

$$\phi = \frac{1}{V_c} \int_{V_c} H(\mathbf{x}, t)\, dV_c, \tag{15}$$

where $V_c = \Delta x \Delta y \Delta z$. By applying equation (15) to (1), the following advection equation for ϕ can be obtained

$$\frac{\partial \phi}{\partial t} + \nabla \cdot (H^{ht} \mathbf{u}_\Gamma) = \phi \nabla \cdot \mathbf{u}_\Gamma. \tag{16}$$

The distinguishing characteristic of each VoF method resides in how to approximate the variable H^{ht}. In this study, we utilize the algebraic volume-of-fluid (VoF) method, employing the Multi-dimensional Tangent Hyperbola reconstruction (MTHINC) [44]. The core concept of MTHINC is to approximate H^{ht} using a hyperbolic tangent function within the cell-containing interface:

$$H^{ht}(\hat{\mathbf{x}}) = \frac{1}{2}\left[1 + \tanh\left(\beta_{th}\left(\mathbb{P}(\hat{\mathbf{x}}) + d_{th}\right)\right)\right], \tag{17}$$

where β_{th}, d_{th} are the sharpness and the normalization parameter, respectively, and $\hat{\mathbf{x}}$ a local coordinate system $\hat{\mathbf{x}} = [(x - x_{i-\frac{1}{2}})/\Delta x, (y - y_{j-\frac{1}{2}})/\Delta y, (z - z_{k-\frac{1}{2}})/\Delta z]$. Initially, the phase indicator H^{ht} is approximated using a polynomial $\mathbb{P}$ of an arbitrary order. Subsequently, the resulting interface between the two phases exhibits a controlled thickness (determined by β_{th}) while maintaining smoothness. This controlled thickness enables accurate computation of the normal vector $\mathbf{n}$ and the curvature tensor κ directly from the scalar function ϕ. More detailed information on the selection of $\mathbb{P}$ and the calculations of d_{th}, $\mathbf{n}$ and κ are found in the original paper [44] and in the open source version of the method [45]. Following the reconstruction process, the interface is transported (from time step n to $n+1$) using a directional splitting method [46,47]. This approach involves sequentially evaluating the numerical fluxes in each direction using, for each split, the latest estimation of the VoF field. Consequently, three preliminary fields $\phi^m_{i,j,k}$ (with $m = [x, y, z]$) are first computed:

$$\phi^m_{i,j,k} = \frac{\phi^s_{i,j,k} - \frac{1}{\Delta l^m}\left[f^m_+(\phi^s_{i,j,k}) - f^m_-(\phi^s_{i,j,k})\right]}{1 - \frac{\Delta t}{\Delta l^m}\left(u^m_{\Gamma_+} - u^m_{\Gamma_-}\right)^n}, \tag{18}$$

where Δt is the time step, $s = [n, x, y]$, $[\Delta l^x, \Delta l^y, \Delta l^z] = [\Delta x, \Delta y, \Delta z]$, $[u^x_\Gamma, u^y_\Gamma, u^z_\Gamma] = [u_\Gamma, v_\Gamma, w_\Gamma]$ with $u^m_{\Gamma_\pm}$ the m-th interface velocity component. The numerical fluxes $f_\pm$ in equation (18) are evaluated using the hyperbolic tangent approximation of H^{ht} as detailed in Ii et al. [44]. Next, the divergence correction step is implemented to enforce volume conservation of both phases at a discrete level:

$$\phi^{n+1}_{i,j,k} = \phi^z_{i,j,k} - \sum_{m=x,y,z} \frac{\Delta t}{\Delta l^m} \phi^m_{i,j,k}\left(u^m_{\Gamma_+} - u^m_{\Gamma_-}\right)^n. \tag{19}$$

The correction term found on the right-hand side of eq. (19) corresponds to the adjustment employed in the conventional approach of directional splitting for a divergence-free advection velocity. In contrast to the original work, where the interface velocity is

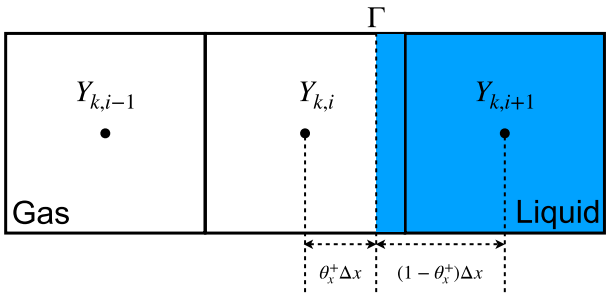

Fig. 2. Computation of the derivative of the mass fraction Y_k^g at the interface with Dirichlet boundary condition $Y_{k,\Gamma}^g$. Γ represents the interface location and θ_x^+ is the normalized distance between the interface and the grid point x_i.

continuous across the interface, the current study considers the presence of phase change. Consequently, an additional correction term is required to accurately account for the non-zero divergence of the interface velocity [29]. This correction term can be expressed as follows:

$$\phi_{i,j,k}^{n+1} = \phi_{i,j,k}^{z} - \sum_{m=x,y,z} \frac{\Delta t}{\Delta l^m} \left(\phi_{i,j,k}^{m} - \phi_{i,j,k}^{n+1} \right) \left(u_{\Gamma_+}^m - u_{\Gamma_-}^m \right)^n. \tag{20}$$

The additional term incorporated into equation (20) can be understood as an implicit volume deflation step [29]. Its purpose is to ensure the utilization of the correct velocity divergence value when updating ϕ to the time level $n+1$. It can be easily shown that this term corresponds to the discrete divergence of $\mathbf{u}_\Gamma$ at time level n; $(\nabla \cdot \mathbf{u}_\Gamma)_{i,j,k}^n$.

3.2. Transport of the vaporized species and interfacial mass flux

The vapor mass transport equation (9) is solved in Ω_2 with the Dirichlet boundary condition imposed at $\mathbf{x} = \mathbf{x}_\Gamma$ reported in eq. (12) (assuming saturation conditions at the interface Γ). The equation is advanced in time explicitly as follows:

$$\frac{Y_k^{g,n+1} - Y_k^{g,n}}{\Delta t} = -\mathbf{u}^n \cdot \nabla Y_k^{g,n} + D_k^g \nabla^2 Y_k^{g,n}. \tag{21}$$

Because the mass fraction Y_k^g is not defined in Ω_1, conventional finite differences are not suitable for directly approximating the interface gradient. To solve the transport equation, the advection term in Eq. (21) is discretized using an upwind scheme; see e.g. [48], and the gradients as below. We treat the spatial discretization in a dimension-by-dimension fashion, and illustrate the methods in the x-direction as an example:

$$\mathbf{u} \cdot \nabla Y_k^g = \frac{(u_i + |u_i|)}{2} \left. \frac{\partial Y_k^g}{\partial x} \right|_{i-\frac{1}{2}} + \frac{(u_i - |u_i|)}{2} \left. \frac{\partial Y_k^g}{\partial x} \right|_{i+\frac{1}{2}}, \tag{22}$$

where u_i is the x-velocity component interpolated into the cell center (i.e. $u_i = (u_{i+1/2,j,k} + u_{i-1/2,j,k})/2$). The gradient of Y_k at $i+1/2$ is computed as follows (the procedure for $i-1/2$ is analogous):

$$\left. \frac{\partial Y_k^g}{\partial x} \right|_{i+\frac{1}{2}} = \frac{Y_{k,i+1}^g - Y_{k,i}^g}{\Delta x}. \tag{23}$$

When the interface crosses a grid cell it is necessary to adjust the spatial discretization near the interface to account for the interface Dirichlet boundary condition. To achieve this, the finite-difference stencil is adapted within grid cells adjacent to the interface. This adaptation involves the creation of a signed distance field (referred to as a level-set field) denoted as ψ, constructed from ϕ using the technique introduced in [49,50]. In this context, values of $\psi > 0$ correspond to region Ω_1, while values of $\psi < 0$ correspond to Ω_2. Consider, for example, a one-dimensional case in which the interface is located between x_i and x_{i+1} as depicted in Fig. 2. The interface is located a distance $(1-\theta_x^+)\Delta x$ from x_{i+1} and $\theta_x^+\Delta x$ from x_i, where θ_x^+ is the distance from the interface to x_i normalized to the range $[0,1]$. The derivative of Y_k at $i+1/2$ is then calculated as follows:

$$\left. \frac{\partial Y_k^g}{\partial x} \right|_{i+\frac{1}{2}} = \frac{Y_{k,\Gamma}^g - Y_{k,i}^g}{\theta_x^+ \Delta x}, \tag{24}$$

where $Y_{k,\Gamma}^g$ is computed from Eqs. (12)-(13), with the interface properties estimated from the neighboring values of ψ:

$$f_{\Gamma,x}^+ = \frac{f_{i+1,j,k}|\psi_{i,j,k}| + f_{i,j,k}|\psi_{i+1,j,k}|}{|\psi_{i,j,k}| + |\psi_{i+1,j,k}|}; \tag{25}$$

in the expression above, f_Γ can be interface temperature T_Γ or interface liquid mass-fraction $Y^l_{k,\Gamma}$. Using the level-set function, the coefficient $\theta^+_x = (x_\Gamma - x_i)/\Delta x$ is computed as proposed in [51]:

$$\theta^+_x = \frac{|\psi_{i,j,k}|}{|\psi_{i+1,j,k}| + |\psi_{i,j,k}|}. \tag{26}$$

In case of small values of $\theta^+_x < 0.25$, the point x_i is removed from the one-sided difference stencil to prevent errors as it approaches a singular value [52]. This leads to the following expression for the derivative of Y_k:

$$\left.\frac{\partial Y^g_k}{\partial x}\right|_{i+\frac{1}{2}} = \frac{Y^g_{k,\Gamma} - Y^g_{k,i-1}}{(\theta^+_x + 1)\Delta x}. \tag{27}$$

As an explicit temporal discretization of Eq. (21) is employed, the second derivatives in the diffusion term are discretized using the first derivatives, previously computed. Taking the term in x as an example, the second derivative reads:

$$\frac{\partial^2 Y^g_k}{\partial x^2} = \frac{1}{\Delta x}\left(\left.\frac{\partial Y^g_k}{\partial x}\right|_{i+\frac{1}{2}} - \left.\frac{\partial Y^g_k}{\partial x}\right|_{i-\frac{1}{2}} \right). \tag{28}$$

The above procedure is performed in a dimension-by-dimension manner for directions y and z. To use Eq. (25), the value of the liquid mass fraction field, Y^l_k, is required in the gas phase (Ω_2), while this field inherently exists only in the liquid phase (Ω_1). An extrapolation approach is therefore employed to extend this field into the gas phase, as detailed in section 3.3. The interfacial mass flux (10)-(11) is computed only in the gas region by projecting the interfacial gradient along the normal direction, wherein the gradient of Y^g_k is computed in a manner akin to the earlier description and adopting a dimension by dimension approach. Note that by employing the procedure here explained, the mass flux $\dot{m}$ is available only on the grid nodes pertaining to the gas region. However, the values of $\dot{m}$ are needed also in some grid points inside the liquid region [39]. Accordingly, $\dot{m}$ is extrapolated over a narrow band around the interface to populate all cells where $|\nabla\phi|_{i,j,k} \neq 0$.

3.3. Transport of the liquid species

The liquid mass fraction fields, denoted as Y^l_k, are defined exclusively in regions where $\psi > 0$ (within the liquid phase subdomain). However, in order to discretize Eq. (9), ghost values are necessary as the finite difference stencil extends across the interface into the gas phase, i.e. where $\psi < 0$. Ghost values are also required in Eq. (12) to compute the vapor mass fraction of the corresponding species at the interface, $Y^g_{k,\Gamma}$. The procedure introduced here aims to provide the necessary ghost values to satisfy the following Robin boundary condition,

$$aY^l_k + b\nabla Y^l_k \cdot \mathbf{n} = f, \tag{29}$$

where a, b and f, in the context of multicomponent evaporation, correspond to $a = \dot{m}$, $b = \rho_g D^g_k$ and $f = \dot{m}_k$, as shown in equation (10). Note here that all the terms in (10) are evaluated at the new time-step $n+1$. Equation (9) is solved in Ω_1 and discretized in time explicitly:

$$\frac{Y^{l,n+1}_k - Y^{l,n}_k}{\Delta t} = -\mathbf{u}^n \cdot \nabla Y^{l,n}_k + D^l_k \nabla^2 Y^{l,n}_k. \tag{30}$$

The advection term is discretized spatially using an upwind scheme. Taking the 1D discretization in x as example, it reads:

$$u\frac{\partial Y^l_k}{\partial x} = \frac{(u_i + |u_i|)}{2}\left.\frac{\partial Y^l_k}{\partial x}\right|_{i-\frac{1}{2}} + \frac{(u_i - |u_i|)}{2}\left.\frac{\partial Y^l_k}{\partial x}\right|_{i+\frac{1}{2}}, \tag{31}$$

where the velocity field is interpolated linearly from the cell face to the cell center (i.e. $u_i = (u_{i+1/2} + u_{i-1/2})/2$). The gradient of Y^l_k at $i + 1/2$ is computed as follows (the procedure for $i - 1/2$ is analogous):

$$\left.\frac{\partial Y^l_k}{\partial x}\right|_{i+\frac{1}{2}} = \frac{Y^l_{k,i+1} - Y^l_{k,i}}{\Delta x}. \tag{32}$$

The second derivatives in the diffusion term are discretized using the first derivatives, previously computed. Taking once more the term in x direction as an example, the second derivative reads:

$$\frac{\partial^2 Y^l_k}{\partial x^2} = \frac{1}{\Delta x}\left(\left.\frac{\partial Y^l_k}{\partial x}\right|_{i+1/2} - \left.\frac{\partial Y^l_k}{\partial x}\right|_{i-1/2} \right). \tag{33}$$

If the interface Γ falls between x_{i+1} and x_i as depicted in Fig. 3, the value $Y^l_{k,i+1}$ is not defined for the cell $x_{1,i+1}$. Hence, a ghost value $Y^{l,G}_{k,i+1}$ should be provided to keep a uniform discretization of Eq. (31) and impose the Robin boundary condition, see [53,1]. This is done in two steps as follows.

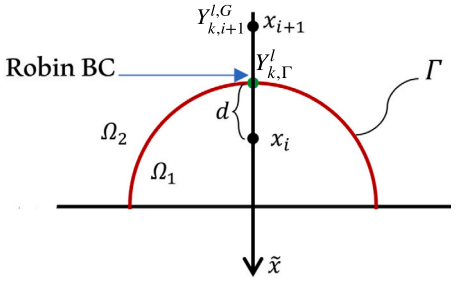

Fig. 3. 2D sketch of Cartesian cell crossed by the interface, Γ. In the plot, $\tilde{x}$ is the signed distance from the reference point on the interface and d is the distance to the interface from the grid point inside the fluid domain. The Robin boundary condition is imposed at the interface location obtained with the reconstructed level-set field.

First, a linear polynomial reconstruction scheme is utilized to calculate the normal derivative of Y^l_k in cells adjacent to the interface. The linear reconstruction along the normal direction takes the form

$$\tilde{Y^l_k}(\tilde{x}) = \omega\tilde{x} + \chi, \tag{34}$$

where ω and χ can be obtained by linear extrapolation of the value on the liquid phase to the interface:

$$\begin{cases} \tilde{Y}^l_k(d) = \omega d + \chi = Y^l_{k,i}, \\ \tilde{Y}^l_k(0) = \chi = Y^l_{k,\Gamma}, \\ \tilde{Y}^{l,\prime}_k(0) = \omega = \dfrac{aY^l_{k,\Gamma} - f}{b}. \end{cases} \tag{35}$$

Here $\tilde{x}$ is the signed distance from the reference point on the interface, $Y^l_{k,\Gamma}$ is the concentration at the interface and d the distance of the first point in the liquid side x_i from the interface, see Fig. 3. Given that the normal vector points from the liquid phase (Ω_1) toward the gas phase (Ω_2), the required normal derivative is essentially identical to $-m$, and can be easily obtained once the coefficients of the linear extrapolation are known from the system in (35), resulting in the following expression:

$$\nabla Y^l_k \cdot \mathbf{n} = -\omega = \frac{f - aY^l_{k,i}}{ad + b}. \tag{36}$$

For the remaining cells, which are not adjacent to the interface, the normal derivative can be directly calculated using a second-order central difference scheme. Consequently, the scalar $Y^l_{k,n}$ can be computed inside the subdomain Ω_1. Note that, in Eq. (36), d can be replaced by the level-set value pertaining to the cells adjacent to the interface, ψ_i.

Secondly, to obtain the ghost values $Y^{l,G}_{k,i+1}$, the normal derivative and the discrete variable, Y^l_k, are extrapolated in the normal direction using a combination of the linear polynomial reconstruction in the normal direction and a second-order PDE extrapolation approach [54]. This approach was originally proposed to extrapolate values from the known subdomain of Y^l_k to the unknown subdomain in the normal direction. It amounts to solving a series of sequential PDEs to the steady state:

$$\frac{\partial Y^l_{k,n}}{\partial \tau} = -\mathcal{H}\nabla Y^l_{k,n} \cdot \mathbf{n}^{pde}, \tag{37}$$

$$\frac{\partial Y^l_k}{\partial \tau} = -\mathcal{H}(\nabla Y^l_k \cdot \mathbf{n}^{pde} - Y^l_{k,n}), \tag{38}$$

where

$$Y^l_{k,n} = \nabla Y^l_k \cdot \mathbf{n}^{pde}, \tag{39}$$

is the directional derivative in the extrapolation direction with $\mathbf{n}^{pde} = \mathbf{n}$ for liquid-to-gas extrapolation and $\mathcal{H}$ is a Heaviside function that keeps the values in the known subdomain (Ω_1) undisturbed and τ is a pseudo time used to advance eqs. (38)-(39) to the steady state solution. An upwind scheme is employed to discretize these PDEs. Once Eqs. (37) and (38) are solved to a steady state iteratively, we obtain the ghost value $Y^{G,l}_{k,i+1}$ in the originally unknown subdomain; this will have a directional derivative equal to the extended $Y^l_{k,n}$ in Eq. (37). The numerical example presented in section 4 demonstrates that the ghost values are second-order accurate.

3.4. Temperature equation

The temperature equation (14) is solved using a whole domain approach. First, a prediction temperature field T^* is computed using the Adams–Bashforth method,

$$T^* = T^n + \Delta t^{n+1}\left(f_{t,1}\mathcal{R}_{\mathcal{T}}^n - f_{t,2}\mathcal{R}_{\mathcal{T}}^{n-1}\right), \tag{40}$$

where $f_{t,1} = (1 + 0.5\Delta t^{n+1}/\Delta t^n)$ and $f_{t,2} = 0.5\Delta t^{n+1}/\Delta t^n$ are the coefficients of the Adams-Bashforth scheme. In equation (40), the operator $\mathcal{R}_{\mathcal{T}}$ includes all the convective and diffusive terms and it is defined below in a semi-discrete form:

$$\mathcal{R}_{\mathcal{T}}^n = -\nabla\cdot(\mathbf{u}^n T^n) + \frac{1}{(\rho c_p)^{n+1}}\nabla\cdot(k^{n+1}\Delta T^n). \tag{41}$$

Next, the source terms in Eq. (14) are included using a first-order Euler scheme,

$$\frac{T^{n+1} - T^*}{\Delta t^{n+1}} = -(\dot{m}\delta_\Gamma)^{n+1}\frac{h_{lv}}{(\rho c_p)^{n+1}} + \sum_{k=1}^{N_v} D_k^g\left(\frac{c_{p,k}^{vap} - c_{p2}}{c_p^{n+1}}\right)\nabla T^*\cdot\nabla Y_k^{g,n+1}(1-\phi^{n+1}), \tag{42}$$

where the arithmetic average is employed for the terms ρc_p and c_p. The spatial discretization technique adopted in this study employs the 5th-order WENO scheme, as outlined in reference [55] and the diffusion term is treated using conventional central differences.

3.5. Interface velocity construction

As a consequence of phase change, the velocity $\mathbf{u}$ in the one-fluid formulation experiences a discontinuity across the interface, which makes it unsuitable to transport the VoF function. Following the approach proposed in [29], we construct an interface velocity for the advection of ϕ in three steps:

1. The Stefan flow velocity $\mathbf{u}_s$ is computed to account for the jump in the flow velocity $\mathbf{u}$ across the interface:

$$\begin{cases}\nabla^2\Psi = \dot{m}\left(\frac{1}{\rho_2} - \frac{1}{\rho_1}\right)|\nabla\phi|,\\ \mathbf{u}_s = \nabla\Psi,\end{cases} \tag{43}$$

   where Ψ denotes the velocity potential, and the Poisson equation for Ψ can be solved using an efficient FFT-based direct solver. The use of direct solvers for equation (43) allows for overcoming potential challenges of stiffness arising from high interfacial mass flux values.
2. The liquid velocity is extended into the gas subdomain by subtracting the Stefan velocity $\mathbf{u}_s$ to the corrected velocity $\mathbf{u}$:

$$\mathbf{u}_{1,e} = \mathbf{u} - \mathbf{u}_s. \tag{44}$$

   Note that $\mathbf{u}_{1,e}$ is divergence-free by construction.
3. The interface velocity $\mathbf{u}_\Gamma$ is finally computed as:

$$\mathbf{u}_\Gamma = \mathbf{u}_{1,e} - \frac{\dot{m}}{\rho_1}\mathbf{n}. \tag{45}$$

   The interface velocity $\mathbf{u}_\Gamma$, as obtained from (45), is then used to advect ϕ, as described in section 3.1. Furthermore, it is worth noting that, similarly to what is commonly done in the prediction/correction procedure for the Navier-Stokes solver, the boundary conditions for Ψ and $\mathbf{u}_{1,e}$ have to be prescribed consistently. They are set to be the same as those of the pressure and prediction velocity, respectively. Additionally, the same boundary conditions used for $\mathbf{u}_{1,e}$ are employed for $\mathbf{u}_\Gamma$.

3.6. Pressure correction algorithm

The two-fluid Navier-Stokes solver employs a projection method [56] along with the pressure-splitting technique outlined in [57]. The primary advantage of this method is the reduction of the variable coefficient Poisson equation, which arises when solving the incompressible Navier-Stokes equations for two-fluid flows. By splitting the variable density pressure-gradient term, the equation can be reduced to a constant coefficient equation. This transformation allows us to use an FFT-based, fast Poisson solver, which is about one order of magnitude faster than a standard iterative solver [58]. It is important to highlight that the numerical model for evaporation proposed here can be readily applied to any conventional two-fluid solvers, without the need to utilize the pressure-splitting technique.

The solution procedure employed in this study utilizes an Adams-Bashforth method to progress the solution from time step n to $n+1$. The semi-discrete form of the procedure is summarized as follows:

$$\left(\frac{\mathbf{u}^{**} - \mathbf{u}^n}{\Delta t^{n+1}}\right) = f_{t,1}\mathcal{R}_{\mathcal{M}}^n - f_{t,2}\mathcal{R}_{\mathcal{M}}^{n-1} + \frac{(\sigma\kappa\mathbf{n}\delta_\Gamma + \hat{\rho}\mathbf{g})^{n+1}}{\rho^{n+1}}, \tag{46}$$

$$\mathbf{u}^{*} = \mathbf{u}^{**} - \frac{\Delta t^{n+1}}{\rho_0}\left[\left(1 - \frac{\rho_0}{\rho^{n+1}}\nabla\hat{p}\right) + \nabla p^{n}\right], \tag{47}$$

$$\nabla^2 \delta p^{n+1} = \frac{\rho_0}{\Delta t^{n+1}}\left[\nabla\cdot\mathbf{u}^{*} - \dot{m}^{n+1}\left(\frac{1}{\rho_2} - \frac{1}{\rho_1}\right)\delta_\Gamma\right], \tag{48}$$

$$\mathbf{u}^{n+1} = \mathbf{u}^{*} - \frac{\Delta t^{n+1}}{\rho_0}\nabla\delta p^{n+1}, \tag{49}$$

$$p^{n+1} = p^{n} + \delta p^{n+1}, \tag{50}$$

where $\mathcal{R}^{n}_{\mathcal{M}}$ and $\mathcal{R}^{n-1}_{\mathcal{M}}$ in equation (46) include the convective and diffusive terms in Eq. (5) computed at the current and previous time levels. $\mathbf{u}^{*}$ denotes the predicted velocity, Δt^{n+1} and Δt^{n} represent the time step computed at time n and $n+1$ to meet the temporal stability requirements, $\rho_0 = \min(\rho_1, \rho_2)$. The intermediate velocity $\mathbf{u}^{**}$ is obtained with the contribution from the terms due to the pressure splitting. Note that $\hat{p}$ represents the time-extrapolated pressure between the current and the old time-step, i.e. $\hat{p} = (1 + \Delta t^{n+1}/\Delta t^{n})p^{n} - (\Delta t^{n+1}/\Delta t^{n})p^{n-1}$. This system of equations is similar to that used in [58], except for the last term of Eq. (48) which incorporates the contribution of phase change to the velocity divergence at the interface, i.e. Eq. (4), regularized over the grid cells where $\delta \neq 0$. The continuum surface force model (CSF) [59] is used for discretizing the surface tension term, which makes the final velocity field numerically differentiable. Nevertheless, due to significant variations in flow velocity across the interface, employing second-order central schemes for the spatial derivative of the convective terms in $\mathcal{R}_{\mathcal{M}}$ is not preferable. Therefore, a *QUICK* scheme [60] is employed for the convective term, while second-order central differences are used for the diffusion terms. The constant coefficient Poisson equation (48)) is solved with a FFT-based solver [37] that can be employed for different combinations of homogeneous pressure boundary conditions. Finally, the velocity field is corrected as in equation (49) to impose the divergence constraint and the pressure is updated as in equation (50).

3.7. Overall solution procedure and time marching

We briefly outline the overall solution procedure in Algorithm 1 for clarity. Furthermore, it is important to note that following each iteration, the time step Δt^{n+1} is updated based on the stability constraints of the entire system:

$$\Delta t^{n+1} = \mathrm{CFL}\ \min(\Delta t_c, \Delta t_\sigma, \Delta t_\mu, \Delta t_e, \Delta t_m)^{n+1}, \tag{51}$$

where Δt_c, Δt_σ, Δt_μ, Δt_e and Δt_m are the maximum allowable time steps due to convention, surface tension, momentum diffusion, thermal energy diffusion, and vapor (also liquid) mass diffusion. These are determined as suggested in [61]:

$$\begin{aligned}
\Delta t_c &= \left(\frac{|u_{x,max}|}{\Delta x} + \frac{|u_{y,max}|}{\Delta y} + \frac{|u_{z,max|}}{\Delta z}\right)^{-1},\\
\Delta t_\sigma &= \left(\frac{(\rho_1+\rho_2)\,min(\Delta x^3, \Delta y^3, \Delta z^3)}{4\pi\sigma}\right)^{0.5},\\
\Delta t_\mu &= \left[\max\left(\frac{\mu_1}{\rho_1}, \frac{\mu_2}{\rho_2}\right)\left(\frac{2}{\Delta x^2} + \frac{2}{\Delta y^2} + \frac{2}{\Delta z^2}\right)\right]^{-1},\\
\Delta t_e &= \left[\max\left(\frac{k_1}{\rho_1 c_{p1}}, \frac{k_2}{\rho_2 c_{p2}}\right)\left(\frac{2}{\Delta x^2} + \frac{2}{\Delta y^2} + \frac{2}{\Delta z^2}\right)\right]^{-1},\\
\Delta t_m &= \left[\max\left(D_k^{l}, D_k^{g}\right)\left(\frac{2}{\Delta x^2} + \frac{2}{\Delta y^2} + \frac{2}{\Delta z^2}\right)\right]^{-1},
\end{aligned} \tag{52}$$

where $|u_{i,max}|$ represents an estimation of ith component of the flow velocity. We have observed that selecting CFL = 0.25 provides a stable and accurate temporal integration.

Algorithm 1 Pseudo-code of the proposed methodology.

1: ϕ, $\mathbf{u}$, p, $Y_k^{l,g}$, T are initialized and n is set to 0.
2: **while** $t < t_{tot}$ **do**
3: Set $n = n+1$ and calculate Δt^{n+1} using Eq. (51).
4: ϕ^{n+1} is calculated from Eq. (20). The generic η and ψ are updated using ϕ^{n+1}.
5: $Y_k^{g,n+1}$, $\dot{m}^{n+1}$ are calculated from Eq. (21) and Eq. (11), respectively.
6: Coefficients of Robin b.c are determined, and $Y_k^{l,n+1}$ is calculated from Eq. (30) as outlined in section 3.3.
7: T^{n+1} is calculated from Eq. (42).
8: Solve the two-fluid Navier-Stokes equations (5) using the pressure-correction Eqs. (46)-(50); $(\mathbf{u}, p)^{n+1}$ are obtained.
9: $\mathbf{u}_\Gamma^{n+1}$ is calculated from Eq. (45) using the constructed divergence-free liquid velocity $\mathbf{u}_{l,e}^{n+1}$.
10: **end while**

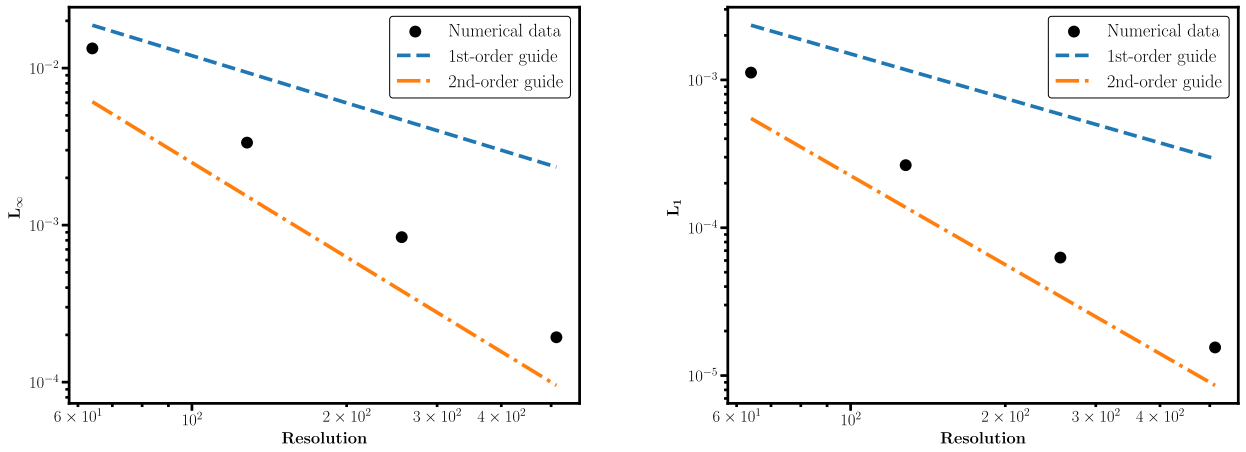

Fig. 4. Error analysis: L^∞ norm (left) and L^1 norm (right) of the error in the solution of the Poisson equation over a circular domain. The dashed lines are first and second-order visual guides. The slopes of the least-square fit of the L^1 and L^∞ error norms are -2.06 and -2.03.

4. Numerical verification and validation

In this section, we present the results of the validation of the proposed numerical algorithm. We first consider a Poisson and Stefan problem to validate the correct imposition of the Robin boundary condition at the interface. Next, we employ an analytical solution for the evaporation of binary droplets to validate the overall numerical algorithm. Furthermore, to test the ability of the code to handle droplet evaporation under deformation, we simulate a sedimenting droplet in a confining container. Finally, the three-dimensional simulation of an evaporating droplet in homogeneous isotropic turbulence is performed.

4.1. Poisson problem over a circular domain

In this test case, we prove that the proposed approach is second-order accurate in imposing a Robin boundary condition at a non-planar domain boundary. To this purpose, we perform a test similar to that in References [53,1]. Specifically, we solve a Poisson equation $\Delta\zeta = g$ over a circular subdomain Ω^+ with radius $R = 0.75$, which is placed at the center of the computational domain $\Omega = [-1,1]\times[-1,1]$. The exact solution $\zeta^{exact} = e^{xy}$ is set within Ω^+ and should be extrapolated into a narrow band in Ω^-. The Robin boundary condition in Eq. (29) is imposed on the interface with $a = 1$ and $b = 1$. The f coefficient becomes in this case $f = a\zeta^{exact} + b\nabla\zeta^{exact}\cdot\vec{n}$. The evolution of the error, measured by the L^1 and L^∞ norm, upon grid refinement is reported in Fig. 4, where it can be seen that the solution is second-order accurate.

The L^1 and L^∞ norms are calculated as follows:

$$\begin{aligned} L^1 &= |\zeta - \zeta^{exact}\|_1 = \sum_{j=1}^{N_y}\sum_{i=1}^{N_x} |\zeta_{i,j} - \zeta_{i,j}^{exact}|, \\ L^\infty &= \|\zeta - \zeta^{exact}\|_\infty = max\,(|\zeta_{i,j} - \zeta_{i,j}^{exact}|), \end{aligned} \tag{53}$$

where N_x and N_y are the number of grid points along the x and y direction.

4.2. Two-dimensional Frank sphere problem with Robin boundary condition

The two-dimensional Frank sphere problem [62] is a classical Stefan problem that describes the growing solidification of a cylinder (in 2D) and a sphere (in 3D). Since it has an exact and explicit solution, the Frank sphere serves as a benchmark for a phase-changing solver where a Dirichlet boundary condition is imposed at the moving interface; however, following the approach proposed in [1], we reformulate the problem so that a Robin boundary condition is employed. The solidification process, where the phase interface expands outwards while keeping its shape, is driven by diffusion, and therefore, the temperature field is governed by the following equation:

$$\frac{\partial T}{\partial t} = k\nabla^2 T. \tag{54}$$

Here, we assume $k = 1$ and $T = 0$ in the solid phase, defined in Ω_1. For the liquid phase, defined in Ω_2, T is given by

$$T = T_\infty\left(1 - \frac{E_1(s^2/4)}{E_1(s_0^2/4)}\right), \tag{55}$$

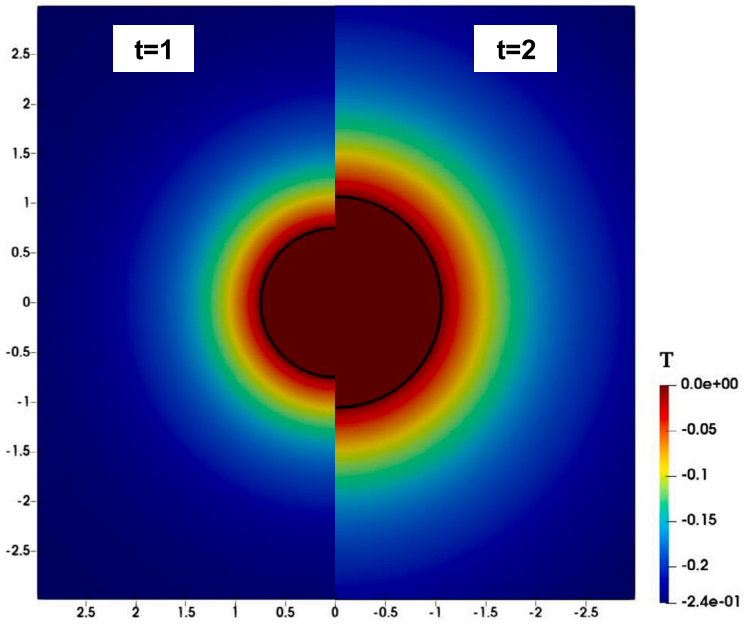

Fig. 5. Contour plot of the temperature fields at $t = 1$ and $t = 2$ for the Frank cylinder problem. The black contour represents the interface location. (For interpretation of the colors in the figure(s), the reader is referred to the web version of this article.)

where $s = rt^{-1/2}$, $r = \sqrt{x^2 + y^2}$ and $E_1(z) = \int_z^\infty \xi^{-1} e^{-\xi} d\xi$, the error function. Note that the far-field temperature T_∞ can be expressed in terms of the initial value of s,

$$T_\infty = -\frac{s_0^2}{4} E_1\left(\frac{s_0^2}{4}\right) e^{\frac{s_0^2}{4}} \tag{56}$$

Once T_∞ is known from (56), the normal derivative of the temperature can be computed as

$$\nabla T \cdot \mathbf{n} = \frac{2T_\infty}{E_1(s_0^2/4)} e^{-s^2/4} s^{-1} t^{-1/2}. \tag{57}$$

Accordingly, the interface velocity immediately follows

$$\mathbf{u}_\Gamma = -\left(\frac{2T_\infty}{E_1(s_0^2/4)} e^{-s^2/4} s^{-1} t^{-1/2}\right) \cdot \mathbf{n}, \tag{58}$$

then used to advect the interface using Eq. (16). See [62] for more details.

Here, we undertake a replication of an experiment akin to the one previously conducted in [53]. A solid disk with an initial radius of $r = 0.75$ is positioned at the center of the computational domain $\Omega = [-3, 3] \times [-3, 3]$. The far-field temperature, denoted as T_∞, is set to -0.246. Along the interface, we apply the Robin boundary condition described in equation (29), with the coefficients $a = 1$ and $b = 1$. The simulation is conducted over the time interval from $t = 1$ to $t = 2$. The temperature fields at time instances $t = 1$ and $t = 2$, with a grid resolution of 256^2, are visually compared in Fig. 5. The visualization shows the gradual transition of supercooled liquid into the solid state, accompanied by the expansion of the interface.

The accuracy of the numerical solution is presented in Figs. 6 and 7 in terms of liquid phase temperature and radius r of the solid region. The radius of the cylinder is computed as $r = \sqrt{A/\pi}$, with A the cross-sectional area retrieved from the VoF field. As expected, both the temperature and radius are first-order accurate due to the approach used to estimate the temperature gradient when estimating the interface velocity, which is also first-order accurate [1].

4.3. Binary droplet evaporation

The proposed methodology is now applied to our problem of interest, i.e. the evaporation of a bi-component droplet. For clarity, the physical parameters defining the different setups are displayed in Table 1. We consider two cases: (i) a static droplet in an isothermal environment in 4.3.1, (ii) a moving droplet which evaporates with thermal effects in 4.3.2.

All material properties in 4.3.1 are chosen to correspond to a Hexadecane-Heptane binary droplet in air at a temperature of $400K$ and pressure of 15 bar, except for the liquid component mass-diffusion rate, which is higher. This choice is made to ensure an almost homogeneous composition for the liquid phase, which is one of the assumptions of the analytical solution we compare our results against in the next subsection.

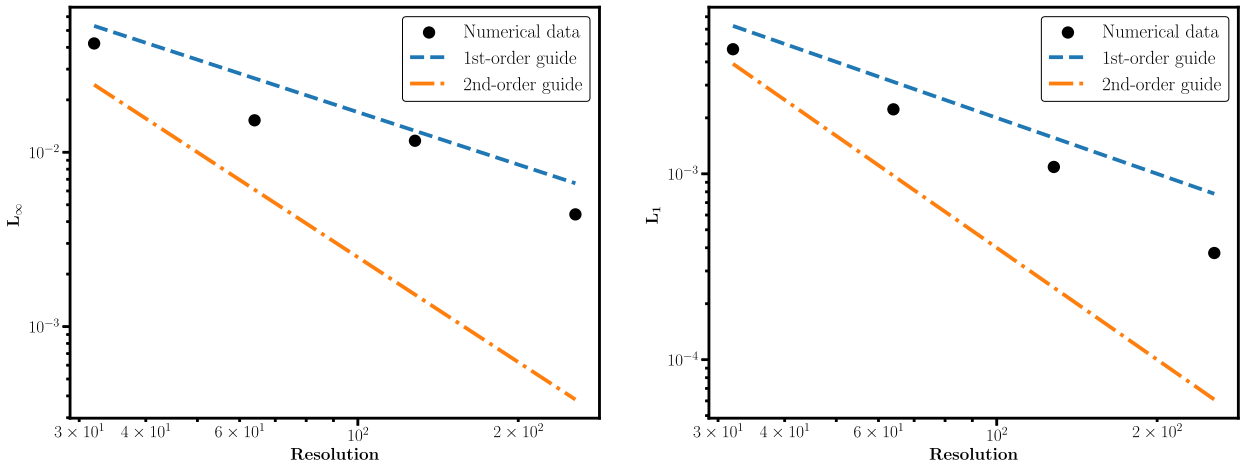

Fig. 6. Error analysis in the L^∞ norm (left) and L^1 norm (right) of the liquid phase temperature for the Frank cylinder problem. The circular markers are numerical data and the dashed lines are first and second-order visual guides.

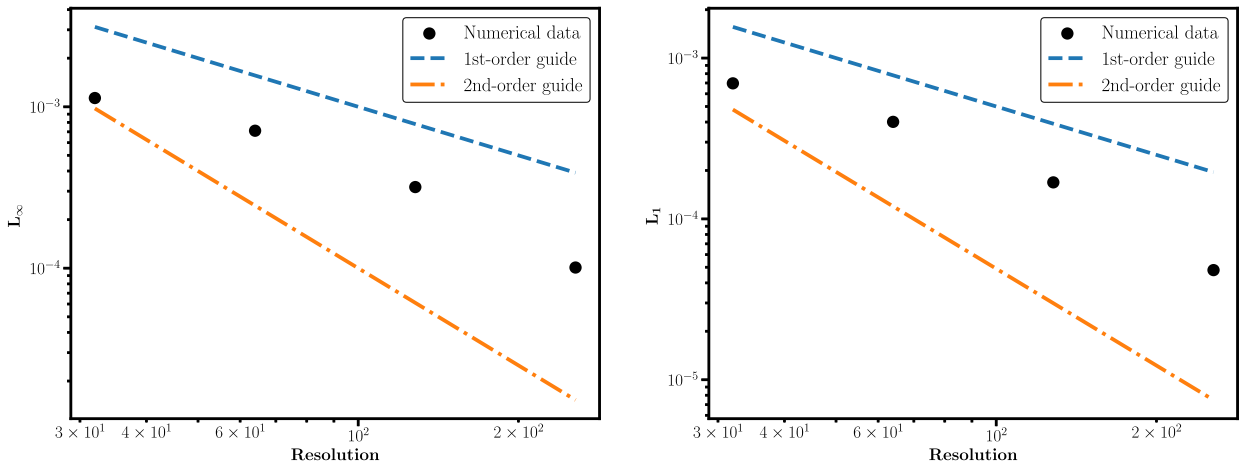

Fig. 7. Error analysis in the L^∞ norm (left) and L^1 norm (right) of the radius of the solid region for the Frank cylinder problem. The circular markers are numerical data and the dashed lines are first and second-order visual guides. The radius is computed by the integral of the VoF field over the whole domain.

Table 1
Governing parameters for the simulations of binary droplet evaporation. The definitions of the different non-dimensional parameters are given in Section 2.4. For all cases $l_{ref} = d_0$, where d_0 is the initial droplet diameter. The mean vapor diffusion coefficient is $\hat{D}_{lg} = Y_1^l D_1^l + (1 - Y_1^l) D_2^{lg}$, where Y_1^l is the initial liquid mass fraction of the specie with lower volatility (i.e. heavier). The other liquid-phase thermophysical properties are calculated using the same analogy. $T_{g,0}$ denotes the initial gas temperature.

Sec.	Re	We	Fr	Pr	Sc_1^g	Sc_2^g	Sc_1^l	Ste	r_ρ	r_μ	r_{c_p}	r_λ	$r_{M,1}$	$r_{M,2}$	u_{ref}	T_{ref}	Y_1^l
4.3.1	0.3	0.1	∞	N/A	3.6	2.1	1.4	N/A	52	27	N/A	N/A	7.8	3.4	$\hat{D}_{lg}/d_0$	N/A	0.9
4.3.2	2.06	0.08	1	0.7	3.6	2.1	var	1.33	30	18.28	4.16	3.23	7.8	3.4	$\sqrt{\lvert\mathbf{g}\rvert d_0}$	$T_{g,0}$	0.1-0.9
4.3.3	-	0.01	N/A	0.7	3.6	2.1	1.0	1.33	48.5	18.28	4.16	3.23	7.8	3.4	U_{rms}	$T_{g,0}$	0.5

4.3.1. *Isothermal droplet evaporation*

This test case considers a binary droplet undergoing isothermal phase change, where a difference between the species concentration at the interface and the domain boundary drives evaporation. Hence, we solve the vapor transport equation (9) with Dirichlet boundary conditions $Y_{k,\infty}^g = 0$ at the domain boundaries and imposed $Y_{k,\Gamma}^g$ at the interface, which is computed from eq. (12). This simple configuration allows us to verify the numerical method for phase-changing two-fluid flows, decoupled from the energy transport equation. The circular droplet has an initial diameter D_0, it is centered in a square domain with dimensions $[-2D_0, 2D_0]^2$, and zero-pressure outflow boundaries. The steady-state solution of the diffusion equation (9) with $\mathbf{u} = 0$ is used as an initial condition for Y_k^g. The other physical parameters are reported in Table 1. We validate our results against the analytical rapid-mixing model by Wilms [63], which provides an analytical solution for two-component droplet evaporation, yielding, in particular, an explicit

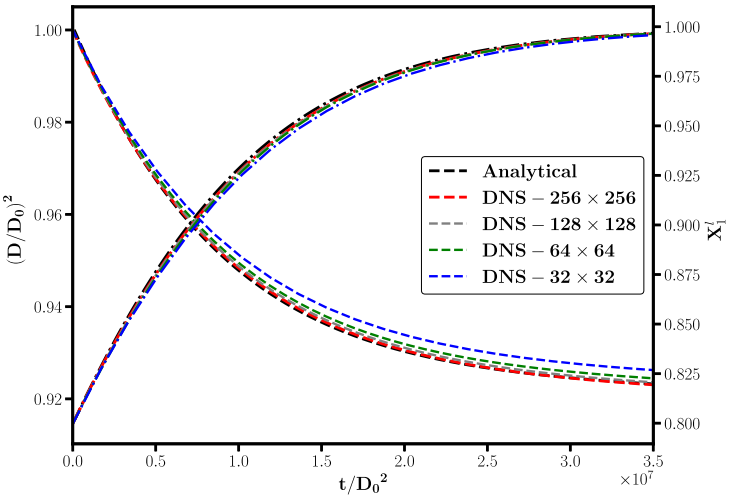

Fig. 8. Comparison of the numerical solution for a bi-component droplet evaporation in quiescent fluid with the analytical solution in [63] based on the rapid-mixing model. The dashed line denotes the dimensionless droplet diameter $(D/D_0)^2$ and the dash-dotted line corresponds to the molar mass-fraction of the less volatile component, X_1^l.

expression for the temporal evolution of the droplet diameter and the droplet composition. The theoretical approach is called the *rapid-mixing model*, as it assumes fast mixing of the different liquids within the droplet so that the liquid mixture is always homogeneous. For completeness, we report below the relations for the droplet diameter and the temporal evolution of droplet composition:

$$\frac{D(X_1^l)}{D_0} = \left[\left(\frac{X_1^l}{X_{1,0}^l} \right)^{\frac{\gamma}{1-\gamma}} \left(\frac{1-X_{1,0}^l}{1-X_1^l} \right)^{\frac{1}{1-\gamma}} \left(\frac{X_1^l - \frac{1}{1-\varepsilon}}{X_{1,0}^l - \frac{1}{1-\varepsilon}} \right) \right]^{\frac{2}{3}}, \tag{59}$$

$$\begin{aligned} t(X_1^l) = -\frac{D_0^2 R^{mol} T}{8 D_1^{lg} p_{1,\Gamma}^{sat} V_1^{mol}} \Bigg[& \left(\frac{1}{1-X_{1,0}^l} \right)^{\frac{2}{3}} - \left(\frac{1}{1-X_1^l} \right)^{\frac{2}{3}} + \frac{2}{3} \ln \left(\frac{(1-X_{1,0}^l)^{\frac{1}{3}} - 1}{(1-X_1^l)^{\frac{1}{3}} - 1} \right) \\ & + \frac{1}{3} \ln \left(\frac{(1-X_1^l)^{\frac{2}{3}} + (1-X_1^l)^{\frac{1}{3}} + 1}{(1-X_{1,0}^l)^{\frac{2}{3}} + (1-X_{1,0}^l)^{\frac{1}{3}} + 1} \right) + \frac{2}{\sqrt{3}} \arctan \left(\frac{2(1-X_1^l)^{\frac{1}{3}} + 1}{\sqrt{3}} \right) \\ & - \frac{2}{\sqrt{3}} \arctan \left(\frac{2(1-X_{1,0}^l)^{\frac{1}{3}} + 1}{\sqrt{3}} \right) \Bigg] \left(\frac{1-X_{1,0}^l}{X_{1,0}^{l,\gamma}} \right)^{\frac{2}{3(1-\gamma)}}, \end{aligned} \tag{60}$$

where X_1^l represents the molar fraction of the heavier component, while $X_{1,0}^l$ denotes its initial molar fraction. The parameter ε is defined as the ratio of the molar volumes (V_1^{mol}/V_2^{mol}) of the pure components and $\gamma = (D_2^g/D_1^g)(p_{2,\Gamma}^{sat}/p_{1,\Gamma}^{sat})$. The analytical solution we refer to assumes the saturation of the species vapor pressure at the droplet interface. This condition is indeed met in our numerical model, where we enforce saturation vapor pressure as a Dirichlet boundary condition at the interface. The accuracy of the analytical solution hinges on the initial molar fraction of the heavier species. In essence, the lower the value of $X_{1,0}^l$, the more precise the analytical solution becomes, see [63] for more details. We, therefore, initialize the droplet composition with $X_{1,0}^l = 0.8$ for our numerical experiment.

Fig. 8 presents the grid convergence study for the time history of the molar mass-fraction of the heavier component with lower volatility, X_1^l, and of the evolution of droplet diameter. The numerical results show excellent agreement with the analytical solution, even for relatively coarse grids. The figure highlights a notable trend: as the concentration of the less volatile component increases, the evaporation rate of the droplet mixture decreases. This process continues until the droplet mainly consists of the low-volatility component (the molar fraction of the heavier component approaches 1), effectively becoming a monocomponent droplet. Thereafter, the decrease of the droplet area $(D/D_0)^2$ becomes linear. A grid convergence study is performed with the global mass conservation error as the target parameter. The global mass conservation error of each species is defined as

$$\varepsilon_{m,k} = \left| \frac{\Delta M_k^{liq} + \Delta M_k^{vap}}{M_{k,0}^{liq}} \right|, \tag{61}$$

where ΔM_k^{liq} and ΔM_k^{vap} denote the species "k" variations as part of the mass of the liquid droplet and in the vapor mass, respectively. These are computed as $\Delta M_k^{liq} = M_{k,0}^{liq} - M_{k,t}^{liq}$ and $\Delta M_k^{vap} = M_{k,0}^{vap} - M_{k,t}^{vap}$, where M_k^{liq} and M_k^{vap} are the species liquid and

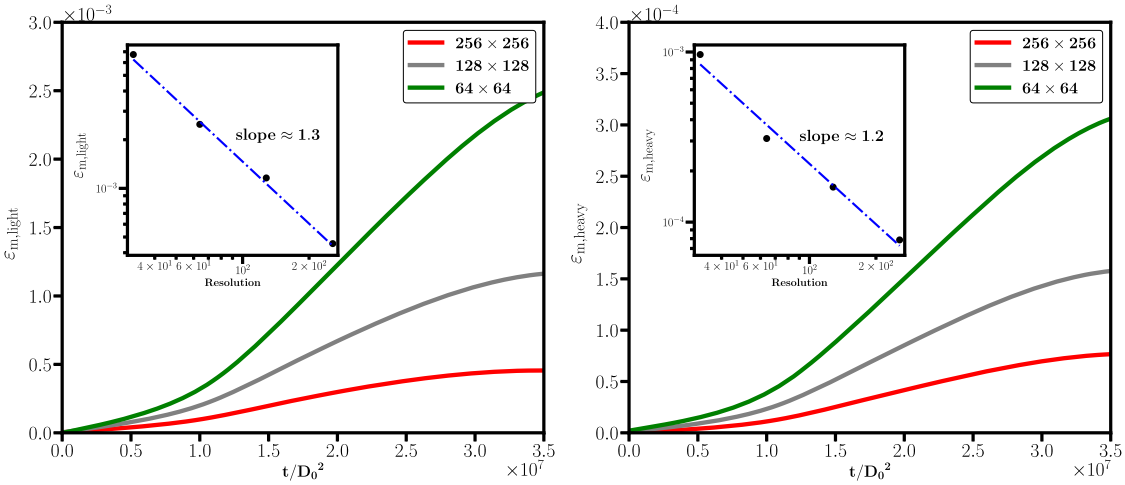

Fig. 9. The mass conservation error of the light (left) and heavy species (right) for different grid resolutions, showing the grid convergence as the grid is refined. The insets show the order of accuracy of the method at $t/D_0^2 = 3.5 \times 10^7$.

vapor masses. The subscript '0' denotes the initial values, and 't' the corresponding variables at time instant t. The mass of each species in the liquid phase is computed as

$$M_k^{liq} = \int_V \rho_l \phi Y_k^l \, dV \tag{62}$$

and the mass of the species in the gas phase as

$$M_k^{gas} = \int_V \rho_g (1-\phi) Y_k^g \, dV + \int_0^t \oint_S \left(\rho_g Y_k^g \, \mathbf{u} + \rho_g D_k^g \nabla Y_k^g \right) \cdot \mathbf{n} \, dS \tag{63}$$

which also accounts for the integration of the convective and diffusive mass fluxes across the domain boundaries. Fig. 9 illustrates the temporal evolution of global mass conservation errors for both the light and heavy components using different grid resolutions. As the grid is refined, the error converges towards zero, highlighting the consistency and grid convergence of our numerical model. Additionally, the insets in the figure display the order of convergence for this particular test case, demonstrating convergence rates above first order.

Next, we display in Fig. 10(a) a visualization of the non-dimensional vapor mass of both species from the simulation at the highest resolution (256×256). The vapor mass fields are only defined within the gas phase, with the highest level of vapor mass at the interface. The results also reveal a higher level of vapor mass for species 2, attributed to its lower Schmidt number. The gradients of these fields are used to compute the interfacial mass flux, which is then extrapolated over a band of about $6\Delta l$ around the interface, see Fig. 10(b) where we depict the dimensionless mass flux. This field is employed to advect the interface in the subsequent step and as a source term in the pressure Poisson equation. Panel (b) also shows the expected velocity field $\mathbf{u}$, with an obvious jump across the interface, Γ. Finally, Fig. 10(c) reports the extrapolated liquid mass fraction of the light component, $Y_1^{l,e}$. This field remains undisturbed and is equal to the liquid mass fraction field inside the droplet; in the gas phase, it is determined through the approach detailed in section 3.3. This extrapolated field is used to update the value of the interfacial vapor mass fraction $Y_{1,\Gamma}^g$ at the next time-step through Eq. (12). The data in panel (c) also confirms the validity of the assumption of a homogeneous droplet mixture.

4.3.2. *Two-dimensional sedimenting droplet in a confined container*

In this section, we consider a two-dimensional sedimenting bicomponent droplet, which evaporates under the action of gravity and deformation. This setup has been proposed in [29], and we reproduce it here in the case of a multicomponent droplet. The purpose is to show that the method has the ability to handle the evaporation of bi-component droplets under deformation, close hydrodynamic interactions with solid boundaries, and large temperature gradients.

The droplet is initially at rest in a domain with dimensions $[0, 2.5d_0] \times [0, 20d_0]$, off-center at the top of the container, with center of mass location $\mathbf{x}_c = [0.625, 18]d_0$. No-slip and no-penetration boundary conditions are imposed at all the boundaries, except for the top boundary, where a zero-pressure outlet is prescribed. Dirichlet boundary conditions for temperature (T_w) and vapor mass fraction ($Y_k^g = 0$) are prescribed at the walls, and (zero) Neumann at the outlet. Additionally, Neumann boundary conditions are enforced on all boundaries for the liquid mass fraction (Y_k^l). The initial temperature field is uniform ($T_0 = 0.75T^{sat} < T_w$), and the initial mass fraction field is set as in the previous section. The remaining relevant flow properties are reported in Table 1. Three configurations of different evaporation rates are studied. In the first two cases, a constant wall temperature is maintained while decreasing the liquid

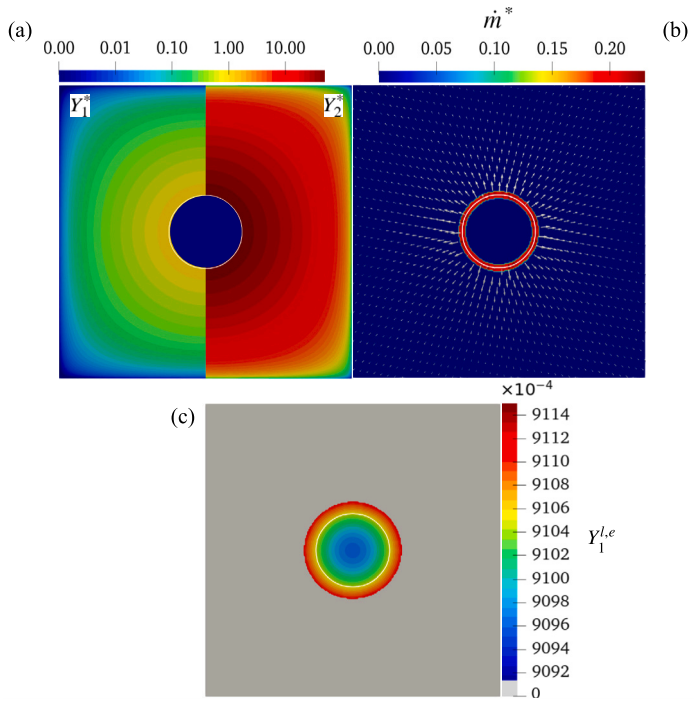

Fig. 10. Isothermal evaporation of a static droplet. (a): contours of the normalized vapor mass fraction fields $Y_k^* = (Y_k^g - Y_{k,\infty}^g)/(Y_{1,\Gamma}^g - Y_{k,\infty}^g)$, where $k = 1$ corresponds to the heavy component and $k = 2$ to the light component; (b): velocity field with contours of the dimensionless interfacial mass flux $\dot{m}^* = \dot{m} d_0/(\rho_2 \hat{D}_g)$ and, (c): contours of the extrapolated liquid mass fraction field at $t\hat{D}_{lg}/d_0^2 = 0.545$. The interface location (i.e. $\phi = 0.5$) is depicted by the solid white line.

mass fraction of the heavier component (Y_1^l), shifting from 0.9 in the initial case to 0.1 in the second case. In the last case, we set $Y_1^l = 0.1$ but with a higher wall temperature. To better characterize the flow condition, we introduce a wall Stefan Ste_w number based on the difference between the imposed wall temperature and the initial temperature, i.e., $\mathrm{Ste}_w \equiv c_{p,2}(T_w - T_0)/h_{lv}$. Note that Ste_w is fixed to 0.026 for the first two cases, while it is increased to $\mathrm{Ste}_w = 0.26$ in the last third case.

Fig. 11(a) illustrates the time history of the droplet position during sedimentation for the three scenarios under examination. Due to the droplet-wall interactions in this confined geometry and the inertia of the droplet, all examples exhibit an oscillatory trajectory. Indeed, the evaporating flow is quenched by the wall, leading to a force on the droplet directed away from it. As the concentration of the droplet's more volatile component increases (first and second case), the evaporation rate also rises, resulting in a stronger wall-repelling force and, consequently, increased droplet oscillation. This effect is especially pronounced in the case with $\mathrm{Ste}_w = 0.26$ and $Y_1^l = 0.1$, where the droplet exhibits significantly greater horizontal displacement compared to the other cases, as depicted in panel (b) where we report the x-coordinate of the droplet center of mass.

Fig. 11(c) shows the time evolution of the droplet total mass, and as expected, the case with higher Ste_w and lower Y_1^l exhibits the highest evaporation rate. The temperature on the side of the droplet closest to the wall is larger than that on the opposite side at early times (as depicted in Fig. 12), hence a stronger Stefan flow, which generates a stronger wall-repelling force. After a while, heat conduction smears out the temperature gradients in the gaseous phase, and the droplet oscillation reduces. Finally, during the later stages, the droplet reaches the bottom of the container with a notable reduction in mass. Nevertheless, the resultant Stefan flow attains a level capable of supporting the droplet's weight, thus causing the droplet to persist in a suspended state similar to the Leidenfrost effect observed in several experiments.

The grid convergence study is shown in Fig. 13 for the configuration with the largest evaporation rate, i.e. $\mathrm{Ste}_w = 0.26$ and $Y_1^l = 0.1$. The results confirm that a resolution of 256×2048 grid points (about 100 grid points over the initial droplet diameter) is necessary to fully resolve the problem.

4.3.3. *Evaporating droplet in isotropic turbulence*

Finally, we perform a simulation for non-isothermal evaporation, initializing a single droplet with an initial diameter of D_0 in homogeneous isotropic turbulence (HIT), where the flow Reynolds number based on the Taylor length-scale is $Re_\lambda \approx 75$. The simulation is conducted in a three-dimensional triply periodic domain of size $\mathcal{L}_x \times \mathcal{L}_y \times \mathcal{L}_z = 4D_0 \times 4D_0 \times 4D_0$, discretized with a uniform grid of size $256 \times 256 \times 256$. A forcing term is added to the right-hand side of eq. (5) to sustain turbulence by injecting energy at large scales. Specifically, we use here the Arnold–Beltrami–Childress (ABC) forcing [64]

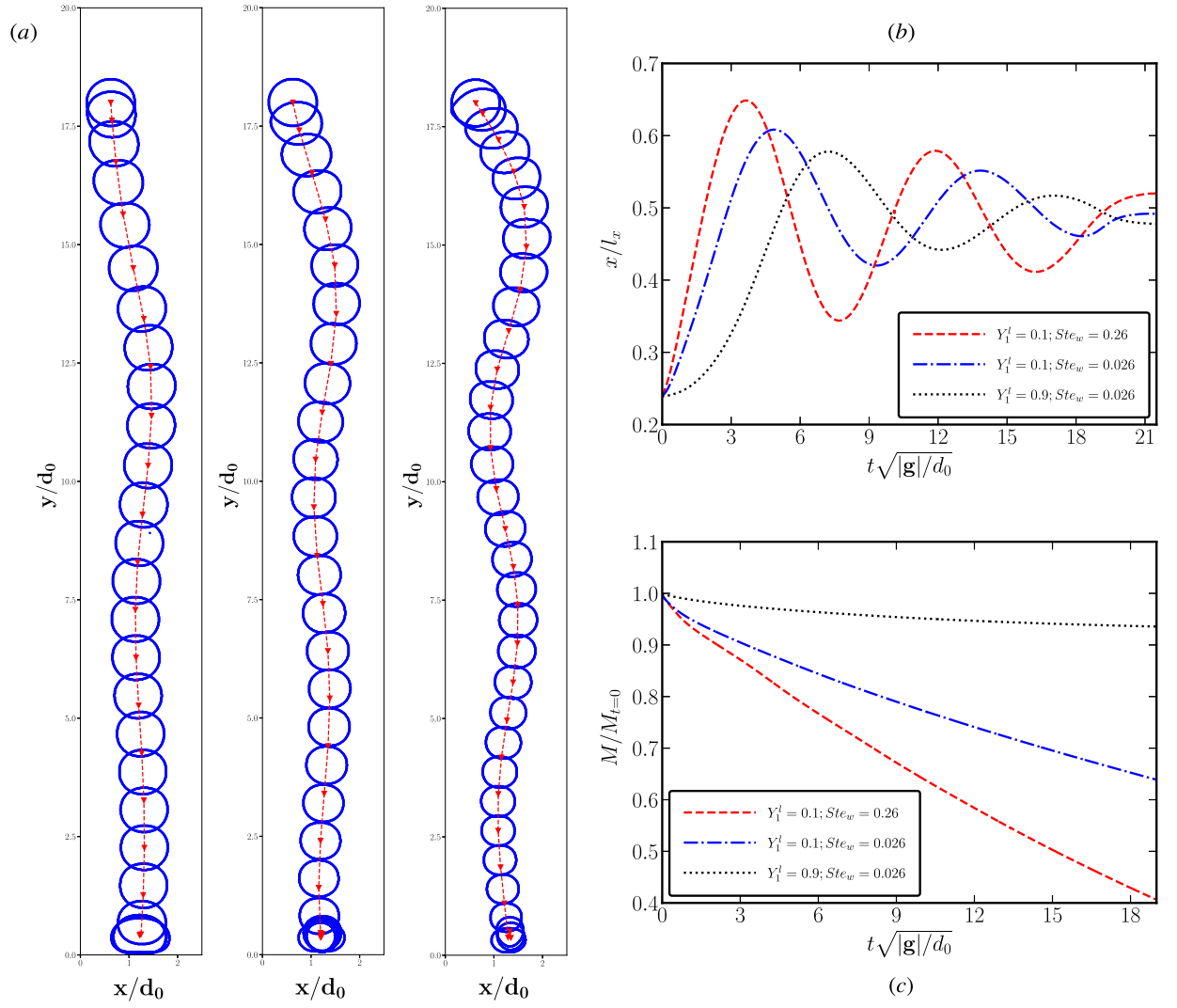

Fig. 11. (a) Trajectory of the droplet's center of mass (red dashed line) for the case of a sedimenting droplet in a confining container from simulations with grid resolution 256×2048. From left to right, the three cases are defined by the liquid mass fraction of species 1 and Stefan number with $Y_1^l = 0.9$ and $\mathrm{Ste}_w = 0.026$; center panel $Y_1^l = 0.1$; $\mathrm{Ste}_w = 0.026$, and $Y_1^l = 0.1$; $\mathrm{Ste}_w = 0.26$. The interface is shown by the solid blue lines with a time interval equal to $0.85\sqrt{d_0/|\mathbf{g}|}$. (b) x-component of the trajectory, (c) history of the droplet mass.

$$\begin{cases} f_x = A\sin k_0 z + C\cos k_0 y, \\ f_y = B\sin k_0 x + A\cos k_0 z, \\ f_z = C\sin k_0 y + B\cos k_0 x, \end{cases} \tag{64}$$

with $x, y, z \in [0, \mathcal{L}_x]$ and $A = B = C = 1$. Energy is injected at wavenumber $k_0 = 2\pi/\mathcal{L}_x = 2$. The initial temperature field is uniform with $T_0 = 0.75T^{sat}$, and the mass fraction field is initialized using the steady state solution of equation (9), as in the previous cases. The surface tension, σ, between the two fluids is selected to achieve an initial turbulent Weber number $We_{rms} = \rho_2 U_{rms}^2 D_0/\sigma = 0.01$, chosen to prevent drop breakup. The remaining governing parameters are detailed in Table 1. In this specific test scenario, we consider constant and uniform density for the gas phase and periodic boundary conditions, which implies a closed system. Hence, given the constant density of each phase, mass conservation requires that $\int_V \nabla\cdot\mathbf{u}dV = 0$. To force the integral of the divergence to be zero in the presence of phase change, we introduce a uniform source term

$$S_v = -\frac{1}{V}\int_V \dot{m}\left(\frac{1}{\rho_2} - \frac{1}{\rho_1}\right)\delta_\Gamma\, dV, \tag{65}$$

as a forcing term in the divergence constraint (4)

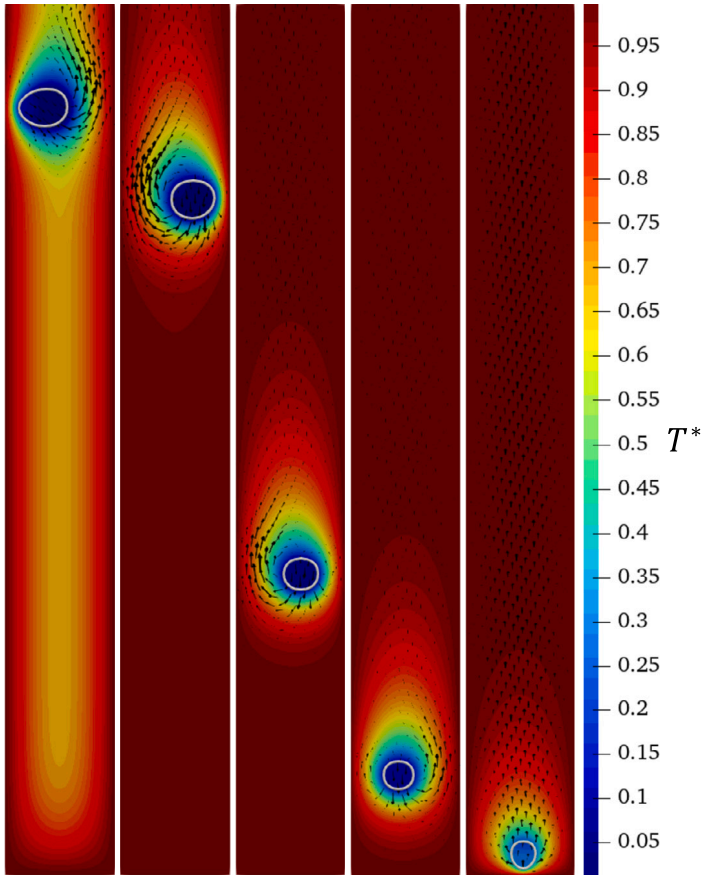

Fig. 12. Isocontour of the normalized temperature ($T^* = (T - T_0)/(T_w - T_0)$) for the case of a sedimenting bi-component droplet ($Y_1^l = 0.1$), in a confining container at $\mathrm{Ste}_w = 0.26$ on a 256×2048 grid. The snapshots are extracted at (from left to right): $t\sqrt{|\mathbf{g}|/d_0} = 1.20$, 3.80, 12.52, 17.66 and 20.79. The interface location is represented by the solid white line.

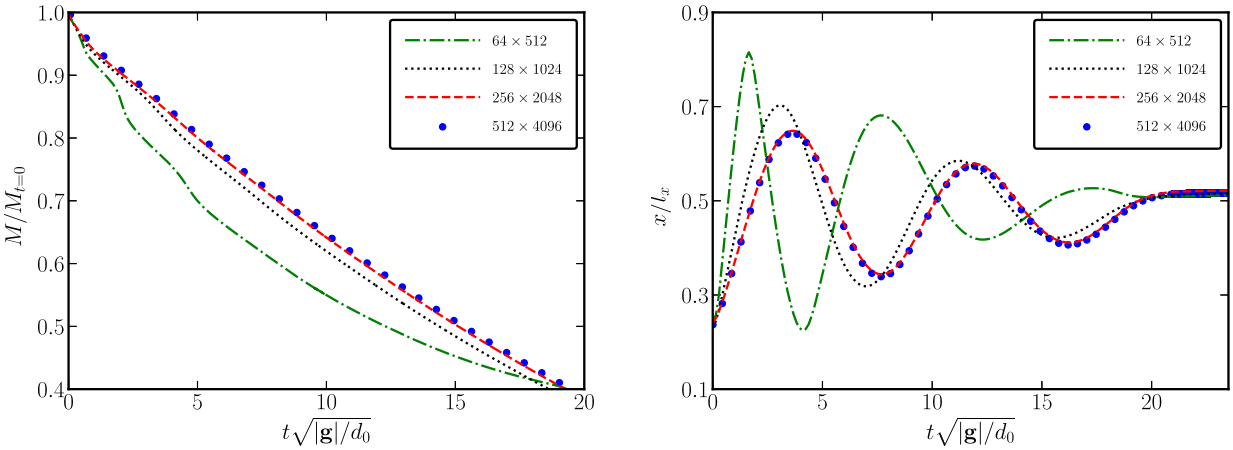

Fig. 13. Grid convergence test for the sedimenting droplet in a confining container with $\mathrm{Ste}_w = 0.26$ and $Y_1^l = 0.1$, (a) time history of the droplet mass, and (b) x-component of the center of mass location, showing oscillations along the container centerline.

$$\nabla \cdot \mathbf{u} = \dot{m} \left(\frac{1}{\rho_2} - \frac{1}{\rho_1} \right) \delta_\Gamma + S_v, \tag{66}$$

which effectively prescribes constant mass in the closed system. Note that this approach is akin to what is often done for prescribing zero net acceleration or no net heating in periodic turbulent channel flows [see, e.g. 65]. For consistency, the same compensation term is added to the right-hand side of the velocity potential Poisson equation, Eq. (43).

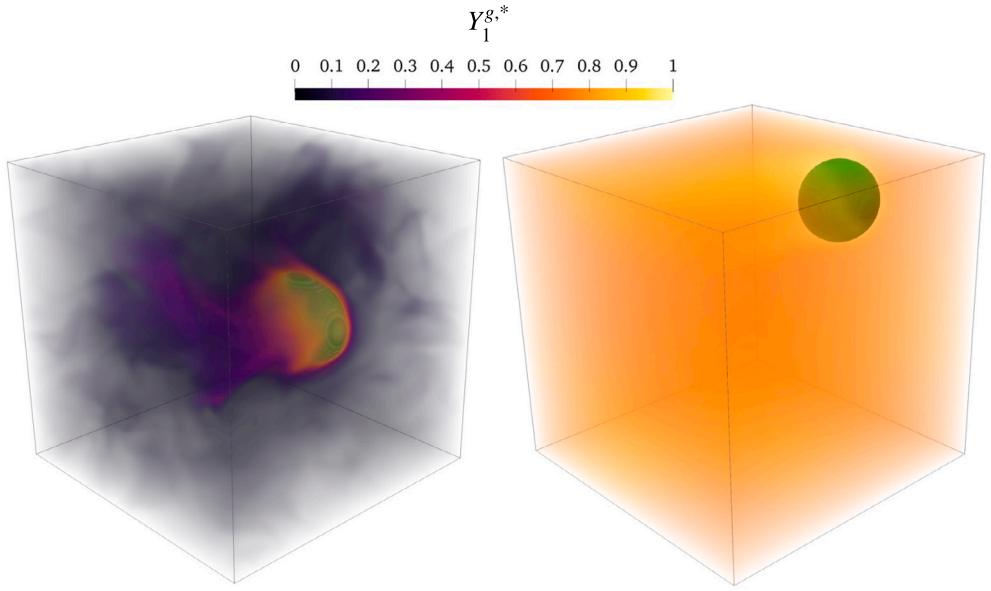

Fig. 14. The translucent surface of normalized vapor mass fraction ($Y_1^{g,*} = Y_1^g / Y_{1,\Gamma}^g$) for the heavy component at two time-instants (from left to right): $tD_1^{lg}/D_0^2 = 0.007$ and 0.307. The solid surface (green) represents the droplet interface ($\phi = 0.5$ contour).

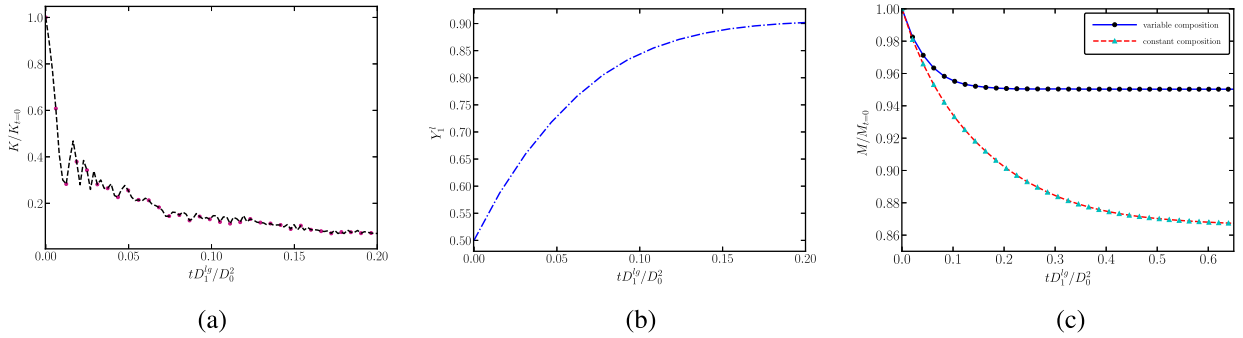

Fig. 15. The time evolution of: (a) the total kinetic energy in the computational domain, K, normalized by its initial value K_0, (b) the heavy component mass fraction Y_1^l, and (c) the normalized droplet mass $M/M_{t=0}$, from simulations with constant droplet composition and variable droplet composition.

We first report a flow visualization. Specifically, we display in Fig. 14 the contours of vapor mass fraction for the heavy component at two different time instants. At the early stage of the simulation, large flow structures disperse vapor around the droplet, enhancing the vapor gradients at the interface and consequently accelerating the evaporation rate. As time evolves, the turbulence decays, as illustrated in Fig. 15(a); hence, the convective transport reduces while the vapor concentration approaches saturation, two effects leading to lower evaporation rates. At the same time, the droplet composition changes until it consists almost uniquely of the heavy component, as indicated by the time history of the droplet composition in Fig. 15(b). The combination of reduced turbulence and slow diffusion of the heavy component almost suppresses the evaporation and the droplet mass reaches a steady configuration, which is illustrated in Fig. 15(c). This figure also compares the evolution of the droplet mass from the simulation introduced above with the results of a similar simulation, where we assume a constant droplet composition. To keep the droplet composition unchanged over time, we decouple Eq. (9) from the rest of the system of equations. As expected, the evaporation rate is faster when the composition is not allowed to change, highlighting the significant role of droplet composition in the evaporation rate. It is important to emphasize that in both simulations, the initial configurations of the liquid mass fraction fields are identical, with the droplet composed of an equal mixture of heavy and light species. Additionally, for the simulation with constant composition, we initialized the droplet properties exactly as in the fully-coupled simulation, where the droplet properties are determined by a composition-weighted average.

Fig. 16 depicts the global mass conservation errors for both light and heavy components over time for different grid resolutions. As the grid is refined, the error steadily decreases, indicating the consistency and grid convergence of our numerical model. Moreover, the insets in the figure indicate the convergence order for this specific test scenario, showcasing convergence rates exceeding first order.

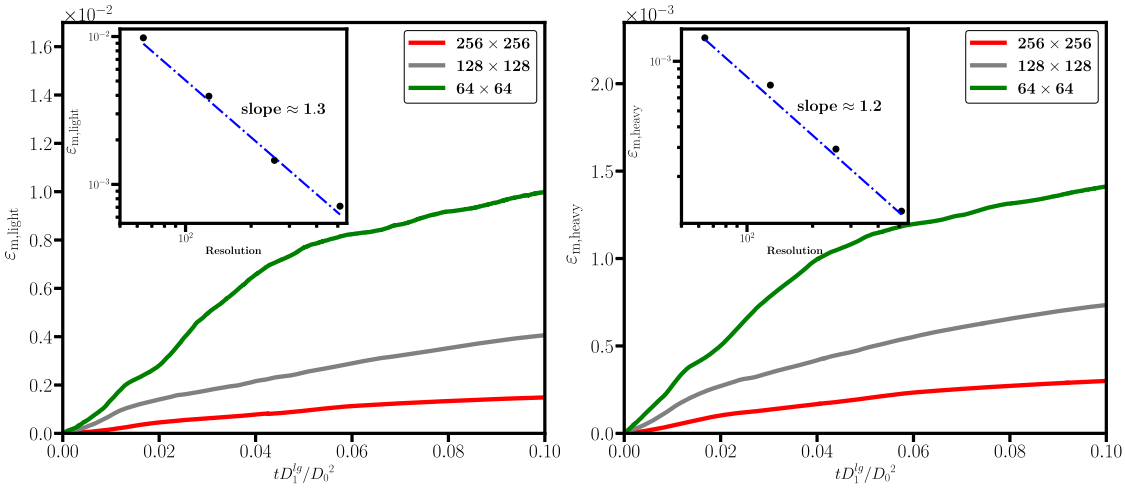

Fig. 16. The mass conservation error of light (left) and heavy species (right) for different grid resolutions, showing grid convergence as the mesh is refined. The insets show the order of accuracy of the method at $tD_1^{lg}/D_0^2 = 0.1$.

5. Conclusion

In this study, we present a novel numerical approach for conducting interface-resolved simulations of multicomponent evaporation in liquid-gas systems. The novelty of the work lies in the approach to couple the transport equations for the vaporized species in the gas phase and the transport equations of the same species in the liquid phase. The first set of equations, valid in the gas phase, is solved with a Dirichlet boundary condition at the moving interface, with the imposed value derived assuming thermodynamic equilibrium at the interface and an equation of state for the local partial pressure (Span-Wagner for the results presented here). The second set of equations for the liquid phase is solved with a Robin boundary condition at the interface, which is formulated to accurately consider the contribution of each vaporized species to the total mass flux. Note that the proposed approach is independent of the chosen method for the interface representation and can be directly employed in other VoF classes, as well as in the level-set and the front-tracking formulations. The algorithm is integrated into an efficient two-fluid solver for evaporating flows, encompassing (1) the transport of the color function for the interface description based on an algebraic VoF method, (2) the solution of the temperature equation, (3) the transport of the vaporized species in the gas phase, (4) the transport of species in the liquid phase, (5) the solution of the momentum equation with a pressure-correction algorithm, and (6) the construction of a smooth interface velocity for the stable and accurate transport of the color function.

The numerical method is rigorously verified against various benchmarks of increasing complexity. Initially, we validate the method using exact solutions for the Poisson and Stefan problem with Robin boundary conditions. Next, we demonstrate excellent agreement between numerical results and analytical solutions for the isothermal evaporation of a binary droplet. Furthermore, we showcase the method's capability to handle large deformations for a droplet evaporating in the presence of walls and demonstrate its potential for three-dimensional simulations of evaporating flows in turbulent environments.

This model provides a distinctive capability for simulating the evaporation of complex liquid mixtures, incorporating thermal effects, and enabling massively parallel simulations of multicomponent evaporating droplets in laminar and turbulent environments. It is noteworthy that enhancing the current implementation by incorporating a conservative form of the energy equation and adopting a momentum-preserving method, as demonstrated in [66], could improve efficiency in solving problems at high-density ratios. Additionally, in line with previous works on single-component evaporation [39,40], relaxing the assumption of constant and uniform thermophysical properties can be considered by adopting a zero-Mach formulation of the governing equations.

CRediT authorship contribution statement

Salar Zamani Salimi: Writing – original draft, Visualization, Validation, Methodology, Investigation, Formal analysis, Conceptualization. **Nicolò Scapin:** Writing – review & editing, Methodology, Conceptualization. **Elena-Roxana Popescu:** Conceptualization. **Pedro Costa:** Writing – review & editing, Supervision. **Luca Brandt:** Writing – review & editing, Supervision, Project administration, Funding acquisition, Conceptualization.

Declaration of competing interest

The authors declare that they have no known competing financial interests or personal relationships that could have appeared to influence the work reported in this paper.

Data availability

Data will be made available on request.

Acknowledgements

The computation resources were provided by the National Infrastructure for High Performance Computing and Data Storage in Norway (project no. NN9561K). Prof. Kun Luo and Prof. Min Chai are acknowledged for the additional clarifications provided on the methodology to implement the Robin boundary condition. Prof. Sebastien Tanguy is acknowledged for fruitful discussions and for pointing to the PhD thesis [42] at the early stage of this work.

Appendix A. Derivation of the interface condition for $Y^g_{k,\Gamma}$

The vaporized mass fraction at the gas side of the interface, $Y^g_{k,\Gamma}$, can be generally defined as:

$$Y^g_{k,\Gamma} = \frac{m^g_{k,\Gamma}}{m_{0,\Gamma} + \sum_{k=1}^{N_v} m^g_{k,\Gamma}}, \tag{A.1}$$

where $m^g_{k,\Gamma}$ and $m_{0,\Gamma}$ are the absolute mass of the species k and of the inert component, both evaluated on the gas side of the interface. If we assume that the mixture of vaporized species behaves as ideal, each absolute mass can be replaced by the corresponding partial pressure p_k using the ideal-gas equation of state, i.e. $p_k V = (m^g_{k,\Gamma}/M_k) R_u T$ where V is the volume of the mixture, R_u is the ideal gas constant and T the temperature. As a result, equation (A.1) reduces to

$$Y^g_{k,\Gamma} = \frac{p_k M_k}{p_0 M_0 + \sum_{k=1}^{N_v} p_k M_k}. \tag{A.2}$$

Using Dalton's law, the partial pressure of the inert p_0 reads $p_0 = p_t - \sum_{k=1}^{N_v} p_k$ with p_t the total pressure of the mixture, which is taken equal to the thermodynamic pressure. Moreover, since the interface is assumed at saturation, p_k can be related to the partial pressure at saturation $p^{sat}_{k,\Gamma}$ by Raoult's law [41], i.e. $p_k = X^l_{k,\Gamma} p^{sat}_{k,\Gamma}$. Accordingly, equation (A.2) finally becomes:

$$Y^g_{k,\Gamma} = \frac{p^{sat}_{k,\Gamma} X^l_{k,\Gamma} M_k}{p_t M_0 + \sum_{k=1}^{N_v} p^{sat}_{k,\Gamma} (M_k - M_0) X^l_{k,\Gamma}}. \tag{A.3}$$

Note that $p^{sat}_{k,\Gamma}$ can be computed as a function of T_Γ using an equation of state, e.g. the Clausius-Clapeyron relation or the Span-Wagner equation of state [41].

References

[1] Min Chai, Kun Luo, Changxiao Shao, Haiou Wang, Jianren Fan, A finite difference discretization method for heat and mass transfer with Robin boundary conditions on irregular domains, J. Comput. Phys. (ISSN 0021-9991) 400 (2020) 108890, https://doi.org/10.1016/j.jcp.2019.108890, https://www.sciencedirect.com/science/article/pii/S0021999119305881.

[2] B. Abramzon, W.A. Sirignano, Droplet vaporization model for spray combustion calculations, Int. J. Heat Mass Transf. (ISSN 0017-9310) 32 (9) (1989) 1605–1618, https://doi.org/10.1016/0017-9310(89)90043-4, https://www.sciencedirect.com/science/article/pii/0017931089900434.

[3] C.K. Law, Recent advances in droplet vaporization and combustion, Prog. Energy Combust. Sci. (ISSN 0360-1285) 8 (3) (1982) 171–201, https://doi.org/10.1016/0360-1285(82)90011-9, https://www.sciencedirect.com/science/article/pii/0360128582900119.

[4] A. Cuoci, M. Mehl, G. Buzzi-Ferraris, T. Faravelli, D. Manca, E. Ranzi, Autoignition and burning rates of fuel droplets under microgravity, Combust. Flame (ISSN 0010-2180) 143 (3) (2005) 211–226, https://doi.org/10.1016/j.combustflame.2005.06.003, https://www.sciencedirect.com/science/article/pii/S0010218005001525.

[5] Juric Damir, Grétar Tryggvason, Computations of boiling flows, Int. J. Multiph. Flow (ISSN 0301-9322) 24 (3) (1998) 387–410, https://doi.org/10.1016/S0301-9322(97)00050-5, https://www.sciencedirect.com/science/article/pii/S0301932297000505.

[6] Asghar Esmaeeli, Grétar Tryggvason, Computations of film boiling. Part I: numerical method, Int. J. Heat Mass Transf. (ISSN 0017-9310) 47 (25) (2004) 5451–5461, https://doi.org/10.1016/j.ijheatmasstransfer.2004.07.027, https://www.sciencedirect.com/science/article/pii/S0017931004002947.

[7] Asghar Esmaeeli, Grétar Tryggvason, Computations of film boiling. Part II: multi-mode film boiling, Int. J. Heat Mass Transf. (ISSN 0017-9310) 47 (25) (2004) 5463–5476, https://doi.org/10.1016/j.ijheatmasstransfer.2004.07.028, https://www.sciencedirect.com/science/article/pii/S0017931004002959.

[8] Grétar Tryggvason, Jiacai Lu, Direct numerical simulations of flows with phase change, in: IUTAM Symposium on Multiphase Flows with Phase Change: Challenges and Opportunities, Proc. IUTAM (ISSN 2210-9838) 15 (2015) 2–13, https://doi.org/10.1016/j.piutam.2015.04.002, https://www.sciencedirect.com/science/article/pii/S2210983815001133.

[9] Muhammad Irfan, Metin Muradoglu, A front tracking method for direct numerical simulation of evaporation process in a multiphase system, J. Comput. Phys. (ISSN 0021-9991) 337 (2017) 132–153, https://doi.org/10.1016/j.jcp.2017.02.036, https://www.sciencedirect.com/science/article/pii/S0021999117301304.

[10] Muhammad Irfan, Metin Muradoglu, A front tracking method for particle-resolved simulation of evaporation and combustion of a fuel droplet, Comput. Fluids (ISSN 0045-7930) 174 (2018) 283–299, https://doi.org/10.1016/j.compfluid.2018.08.007, https://www.sciencedirect.com/science/article/pii/S0045793018304857.

[11] Jiacai Lu, Gretar Tryggvason, Direct numerical simulations of multifluid flows in a vertical channel undergoing topology changes, Phys. Rev. Fluids 3 (8) (2018) 084401.
[12] Jiacai Lu, Gretar Tryggvason, Multifluid flows in a vertical channel undergoing topology changes: effect of void fraction, Phys. Rev. Fluids 4 (8) (2019) 084301.
[13] Muhammad Nufail Farooqi, Daulet Izbassarov, Metin Muradoğlu, Didem Unat, Communication analysis and optimization of 3d front tracking method for multiphase flow simulations, Int. J. High Perform. Comput. Appl. 33 (1) (2019) 67–80.
[14] G. Son, V.K. Dhir, Numerical simulation of film boiling near critical pressures with a level set method, J. Heat Transf. (ISSN 0022-1481) 120 (1) (1998) 183–192, https://doi.org/10.1115/1.2830042.
[15] Frédéric Gibou, Ronald Fedkiw, A fourth order accurate discretization for the Laplace and heat equations on arbitrary domains, with applications to the Stefan problem, J. Comput. Phys. (ISSN 0021-9991) 202 (2) (2005) 577–601, https://doi.org/10.1016/j.jcp.2004.07.018, https://www.sciencedirect.com/science/article/pii/S0021999104002980.
[16] Sébastien Tanguy, Michaël Sagan, Benjamin Lalanne, Frédéric Couderc, Catherine Colin, Benchmarks and numerical methods for the simulation of boiling flows, J. Comput. Phys. (ISSN 0021-9991) 264 (2014) 1–22, https://doi.org/10.1016/j.jcp.2014.01.014, https://www.sciencedirect.com/science/article/pii/S0021999114000412.
[17] Moon Soo Lee, Amir Riaz, Vikrant Aute, Direct numerical simulation of incompressible multiphase flow with phase change, J. Comput. Phys. (ISSN 0021-9991) 344 (2017) 381–418, https://doi.org/10.1016/j.jcp.2017.04.073, https://www.sciencedirect.com/science/article/pii/S0021999117303613.
[18] Sébastien Tanguy, Thibaut Ménard, Alain Berlemont, A level set method for vaporizing two-phase flows, J. Comput. Phys. (ISSN 0021-9991) 221 (2) (2007) 837–853, https://doi.org/10.1016/j.jcp.2006.07.003, https://www.sciencedirect.com/science/article/pii/S0021999106003214.
[19] Lucia Rueda Villegas, Romain Alis, Mathieu Lepilliez, Sébastien Tanguy, A ghost fluid/level set method for boiling flows and liquid evaporation: application to the Leidenfrost effect, J. Comput. Phys. (ISSN 0021-9991) 316 (2016) 789–813, https://doi.org/10.1016/j.jcp.2016.04.031, https://www.sciencedirect.com/science/article/pii/S0021999116300778.
[20] Kun Luo, Changxiao Shao, Min Chai, Jianren Fan, Level set method for atomization and evaporation simulations, Prog. Energy Combust. Sci. (ISSN 0360-1285) 73 (2019) 65–94, https://doi.org/10.1016/j.pecs.2019.03.001, https://www.sciencedirect.com/science/article/pii/S0360128518301710.
[21] Min Chai, Kun Luo, Changxiao Shao, Haiou Wang, Jianren Fan, Interface-resolved detailed numerical simulation of evaporating two-phase flows with Robin boundary conditions on irregular domains, Int. J. Heat Mass Transf. (ISSN 0017-9310) 145 (2019) 118774, https://doi.org/10.1016/j.ijheatmasstransfer.2019.118774, https://www.sciencedirect.com/science/article/pii/S0017931019331813.
[22] Kun Luo, Changxiao Shao, Yue Yang, Jianren Fan, A mass conserving level set method for detailed numerical simulation of liquid atomization, J. Comput. Phys. (ISSN 0021-9991) 298 (2015) 495–519, https://doi.org/10.1016/j.jcp.2015.06.009, https://www.sciencedirect.com/science/article/pii/S0021999115003952.
[23] Zhouyang Ge, Jean-Christophe Loiseau, Outi Tammisola, Luca Brandt, An efficient mass-preserving interface-correction level set/ghost fluid method for droplet suspensions under depletion forces, J. Comput. Phys. (ISSN 0021-9991) 353 (2018) 435–459, https://doi.org/10.1016/j.jcp.2017.10.046, https://www.sciencedirect.com/science/article/pii/S0021999117308136.
[24] O. Ubbink, R.I. Issa, A method for capturing sharp fluid interfaces on arbitrary meshes, J. Comput. Phys. (ISSN 0021-9991) 153 (1) (1999) 26–50, https://doi.org/10.1006/jcph.1999.6276, https://www.sciencedirect.com/science/article/pii/S0021999199962769.
[25] Duong A. Hoang, Volkert van Steijn, Luis M. Portela, Michiel T. Kreutzer, Chris R. Kleijn, Benchmark numerical simulations of segmented two-phase flows in microchannels using the volume of fluid method, Comput. Fluids (ISSN 0045-7930) 86 (2013) 28–36, https://doi.org/10.1016/j.compfluid.2013.06.024, https://www.sciencedirect.com/science/article/pii/S0045793013002612.
[26] Jan Schlottke, Bernhard Weigand, Direct numerical simulation of evaporating droplets, J. Comput. Phys. (ISSN 0021-9991) 227 (10) (2008) 5215–5237, https://doi.org/10.1016/j.jcp.2008.01.042, https://www.sciencedirect.com/science/article/pii/S0021999108000740.
[27] Jonathan Reutzsch, Corine Kieffer-Roth, Bernhard Weigand, A consistent method for direct numerical simulation of droplet evaporation, J. Comput. Phys. (ISSN 0021-9991) 413 (2020) 109455, https://doi.org/10.1016/j.jcp.2020.109455, https://www.sciencedirect.com/science/article/pii/S0021999120302291.
[28] C. Ma, D. Bothe, Numerical modeling of thermocapillary two-phase flows with evaporation using a two-scalar approach for heat transfer, J. Comput. Phys. (ISSN 0021-9991) 233 (2013) 552–573, https://doi.org/10.1016/j.jcp.2012.09.011, https://www.sciencedirect.com/science/article/pii/S0021999112005426.
[29] Nicolò Scapin, Pedro Costa, Luca Brandt, A volume-of-fluid method for interface-resolved simulations of phase-changing two-fluid flows, J. Comput. Phys. (ISSN 0021-9991) 407 (2020) 109251, https://doi.org/10.1016/j.jcp.2020.109251, https://www.sciencedirect.com/science/article/pii/S0021999120300255.
[30] L.C. Malan, A.G. Malan, S. Zaleski, P.G. Rousseau, A geometric vof method for interface resolved phase change and conservative thermal energy advection, J. Comput. Phys. (ISSN 0021-9991) 426 (2021) 109920, https://doi.org/10.1016/j.jcp.2020.109920, https://www.sciencedirect.com/science/article/pii/S002199912030694X.
[31] John Palmore, Olivier Desjardins, A volume of fluid framework for interface-resolved simulations of vaporizing liquid-gas flows, J. Comput. Phys. (ISSN 0021-9991) 399 (2019) 108954, https://doi.org/10.1016/j.jcp.2019.108954, https://www.sciencedirect.com/science/article/pii/S002199911930659X.
[32] Victor Boniou, Thomas Schmitt, Aymeric Vié, Consistency and accuracy in the simulation of two-phase flows with phase change using sharp interface capturing methods, J. Comput. Phys. (ISSN 0021-9991) 470 (2022) 111604, https://doi.org/10.1016/j.jcp.2022.111604, https://www.sciencedirect.com/science/article/pii/S0021999122006660.
[33] Edoardo Cipriano, Alessio Frassoldati, Tiziano Faravelli, Stéphane Popinet, Alberto Cuoci, et al., Multicomponent droplet evaporation in a geometric volume-of-fluid framework, J. Comput. Phys. 507 (2024) 112955.
[34] Gabriele Gennari, Richard Jefferson-Loveday, Stephen J. Pickering, A phase-change model for diffusion-driven mass transfer problems in incompressible two-phase flows, Chem. Eng. Sci. 259 (2022) 117791.
[35] Bradley Boyd, Yue Ling, A consistent volume-of-fluid approach for direct numerical simulation of the aerodynamic breakup of a vaporizing drop, Comput. Fluids 254 (2023) 105807.
[36] Bradley Boyd, Sid Becker, Yue Ling, Simulation and modeling of the vaporization of a freely moving and deforming drop at low to moderate Weber numbers, Int. J. Heat Mass Transf. 218 (2024) 124735.
[37] Pedro Costa, A fft-based finite-difference solver for massively-parallel direct numerical simulations of turbulent flows, Comput. Math. Appl. (ISSN 0898-1221) 76 (8) (2018) 1853–1862, https://doi.org/10.1016/j.camwa.2018.07.034, https://www.sciencedirect.com/science/article/pii/S089812211830405X.
[38] Grétar Tryggvason, Ruben Scardovelli, Stéphane Zaleski, Direct Numerical Simulations of Gas–Liquid Multiphase Flows, Cambridge University Press, 2011.
[39] Nicolò Scapin, Federico Dalla Barba, Giandomenico Lupo, Marco Edoardo Rosti, Christophe Duwig, Luca Brandt, Finite-size evaporating droplets in weakly compressible homogeneous shear turbulence, J. Fluid Mech. 934 (2022) A15, https://doi.org/10.1017/jfm.2021.1140.
[40] Nicolò Scapin, Andreas D. Demou, Luca Brandt, Evaporating Rayleigh–Bénard convection: prediction of interface temperature and global heat transfer modulation, J. Fluid Mech. 957 (2023) A12.
[41] Robert C. Reid, John M. Prausnitz, Bruce E. Poling, The Properties of Gases and Liquids, 1987.
[42] Alis Romain, Simulation numérique directe de gouttes et de groupes de gouttes qui s' évaporent dans un écoulement laminaire ou turbulent, PhD thesis, ISAE, Toulouse, 2018.
[43] Roland Span, Wolfgang Wagner, A new equation of state for carbon dioxide covering the fluid region from the triple-point temperature to 1100 k at pressures up to 800 mpa, J. Phys. Chem. Ref. Data 25 (6) (1996) 1509–1596.
[44] Satoshi Ii, Kazuyasu Sugiyama, Shintaro Takeuchi, Shu Takagi, Yoichiro Matsumoto, Feng Xiao, An interface capturing method with a continuous function: the thinc method with multi-dimensional reconstruction, J. Comput. Phys. (ISSN 0021-9991) 231 (5) (2012) 2328–2358, https://doi.org/10.1016/j.jcp.2011.11.038, https://www.sciencedirect.com/science/article/pii/S0021999111006942.

[45] Marco Crialesi-Esposito, Nicolò Scapin, Andreas D. Demou, Marco Edoardo Rosti, Pedro Costa, Filippo Spiga, Luca Brandt, Flutas: a gpu-accelerated finite difference code for multiphase flows, Comput. Phys. Commun. 284 (2023) 108602.
[46] Elbridge Gerry Puckett, Ann S. Almgren, John B. Bell, Daniel L. Marcus, William J. Rider, A high-order projection method for tracking fluid interfaces in variable density incompressible flows, J. Comput. Phys. (ISSN 0021-9991) 130 (2) (1997) 269–282, https://doi.org/10.1006/jcph.1996.5590, https://www.sciencedirect.com/science/article/pii/S0021999196955904.
[47] Eugenio Aulisa, Sandro Manservisi, Ruben Scardovelli, Stephane Zaleski, A geometrical area-preserving volume-of-fluid advection method, J. Comput. Phys. (ISSN 0021-9991) 192 (1) (2003) 355–364, https://doi.org/10.1016/j.jcp.2003.07.003, https://www.sciencedirect.com/science/article/pii/S0021999103003759.
[48] Yohei Sato, Bojan Ničeno, A sharp-interface phase change model for a mass-conservative interface tracking method, J. Comput. Phys. (ISSN 0021-9991) 249 (2013) 127–161, https://doi.org/10.1016/j.jcp.2013.04.035, https://www.sciencedirect.com/science/article/pii/S0021999113003197.
[49] A. Albadawi, D.B. Donoghue, A.J. Robinson, D.B. Murray, Y.M.C. Delauré, Influence of surface tension implementation in volume of fluid and coupled volume of fluid with level set methods for bubble growth and detachment, Int. J. Multiph. Flow (ISSN 0301-9322) 53 (2013) 11–28, https://doi.org/10.1016/j.ijmultiphaseflow.2013.01.005, https://www.sciencedirect.com/science/article/pii/S0301932213000190.
[50] Giovanni Russo, Peter Smereka, A remark on computing distance functions, J. Comput. Phys. (ISSN 0021-9991) 163 (1) (2000) 51–67, https://doi.org/10.1006/jcph.2000.6553, https://www.sciencedirect.com/science/article/pii/S0021999100965537.
[51] Xu-Dong Liu, Ronald P. Fedkiw, Myungjoo Kang, A boundary condition capturing method for Poisson's equation on irregular domains, J. Comput. Phys. (ISSN 0021-9991) 160 (1) (2000) 151–178, https://doi.org/10.1006/jcph.2000.6444, https://www.sciencedirect.com/science/article/pii/S0021999100964441.
[52] M. Dodd, Direct numerical simulation of droplet-laden isotropic turbulence, http://hdl.handle.net/1773/40466, 2017.
[53] Joseph Papac, Frédéric Gibou, Christian Ratsch, Efficient symmetric discretization for the Poisson, heat and Stefan-type problems with Robin boundary conditions, J. Comput. Phys. (ISSN 0021-9991) 229 (3) (2010) 875–889, https://doi.org/10.1016/j.jcp.2009.10.017, https://www.sciencedirect.com/science/article/pii/S0021999109005622.
[54] Tariq D. Aslam, A partial differential equation approach to multidimensional extrapolation, J. Comput. Phys. (ISSN 0021-9991) 193 (1) (2004) 349–355, https://doi.org/10.1016/j.jcp.2003.08.001, https://www.sciencedirect.com/science/article/pii/S0021999103004170.
[55] Marcos Castro, Bruno Costa, Wai Sun Don, High order weighted essentially non-oscillatory weno-z schemes for hyperbolic conservation laws, J. Comput. Phys. (ISSN 0021-9991) 230 (5) (2011) 1766–1792, https://doi.org/10.1016/j.jcp.2010.11.028, https://www.sciencedirect.com/science/article/pii/S0021999110006431.
[56] A.J. Chorin, Numerical solution of the Navier-Stokes equations, Math. Comput. 22 (104) (1968) 745–762, https://doi.org/10.1090/S0025-5718-1968-0242392-2.
[57] S. Dong, J. Shen, A time-stepping scheme involving constant coefficient matrices for phase-field simulations of two-phase incompressible flows with large density ratios, J. Comput. Phys. (ISSN 0021-9991) 231 (17) (2012) 5788–5804, https://doi.org/10.1016/j.jcp.2012.04.041, https://www.sciencedirect.com/science/article/pii/S0021999112002239.
[58] Michael S. Dodd, Antonino Ferrante, A fast pressure-correction method for incompressible two-fluid flows, J. Comput. Phys. (ISSN 0021-9991) 273 (2014) 416–434, https://doi.org/10.1016/j.jcp.2014.05.024, https://www.sciencedirect.com/science/article/pii/S0021999114003702.
[59] J.U. Brackbill, D.B. Kothe, C. Zemach, A continuum method for modeling surface tension, J. Comput. Phys. (ISSN 0021-9991) 100 (2) (1992) 335–354, https://doi.org/10.1016/0021-9991(92)90240-Y, https://www.sciencedirect.com/science/article/pii/002199919290240Y.
[60] B.P. Leonard, A stable and accurate convective modelling procedure based on quadratic upstream interpolation, Comput. Methods Appl. Mech. Eng. (ISSN 0045-7825) 19 (1) (1979) 59–98, https://doi.org/10.1016/0045-7825(79)90034-3, https://www.sciencedirect.com/science/article/pii/0045782579900343.
[61] M. Kang, R.P. Fedkiw, X.-D. Liu, A boundary condition capturing method for multiphase incompressible flow, J. Sci. Comput. 15 (3) (2000) 323–360, https://doi.org/10.1023/A:1011178417620, https://www.scopus.com/inward/record.uri?eid=2-s2.0-0034260316&doi=10.1023%2fA%3a1011178417620&partnerID=40&md5=dbf11350c30116e0dd70fdbdc1ee3a49.
[62] F.C. Frank, Radially symmetric phase growth controlled by diffusion, Proc. R. Soc. Lond. Ser. A 201 (1067) (May 1950) 586–599, https://doi.org/10.1098/rspa.1950.0080.
[63] Jochen Wilms, Evaporation of multicomponent droplets, PhD thesis, 2005, https://doi.org/10.18419/opus-3711.
[64] P.D. Mininni, A. Alexakis, A. Pouquet, Large-scale flow effects, energy transfer, and self-similarity on turbulence, Phys. Rev. E 74 (Jul 2006) 016303, https://doi.org/10.1103/PhysRevE.74.016303, https://link.aps.org/doi/10.1103/PhysRevE.74.016303.
[65] Sergio Pirozzoli, Matteo Bernardini, Paolo Orlandi, Passive scalars in turbulent channel flow at high Reynolds number, J. Fluid Mech. 788 (2016) 614–639.
[66] T. Arrufat, M. Crialesi-Esposito, D. Fuster, Y. Ling, L. Malan, S. Pal, R. Scardovelli, G. Tryggvason, S. Zaleski, A mass-momentum consistent, volume-of-fluid method for incompressible flow on staggered grids, Comput. Fluids (ISSN 0045-7930) 215 (2021) 104785, https://doi.org/10.1016/j.compfluid.2020.104785, https://www.sciencedirect.com/science/article/pii/S0045793020303558.